# DEVELOPMENT OF STEEL-ALUMINA COMPOSITES FOR WEAR APPLICATIONS

Catherine Kuforiji

A Thesis Submitted to the
Faculty of Graduate and Postdoctoral Studies
In partial fulfillment of the requirements for the degree of

**DOCTOR OF PHILOSOPHY**

in Mechanical Engineering

Ottawa-Carleton Institute for Mechanical and Aerospace Engineering
Faculty of Engineering
University of Ottawa
Ottawa, Canada.
May 2017

## ABSTRACT

Ceramic-metal matrix composites produced by powder metallurgy provide a solution in engineering applications where materials with high wear resistance are required. In the mining industry, the wear of materials is a crucial and widely recognized industrial problem as over 50 % of components fail as a result of wear damage. Increasing the wear resistance of these components will contribute to a reduction in maintenance and thereby increase efficiency.

In this present research, SS316L-50wt.% $Al_2O_3$ composites were fabricated using the powder metallurgy route. The effects of the powder metallurgy processing parameters were studied. The produced cermet composites were characterized with respect to microstructure, density, hardness and toughness. Furthermore, the wear behavior of the composites was studied using pin-on-disc testing under dry sliding conditions. The produced test results were used to improve existing wear models, particularly the Wayne's model.

The highest hardness of 1085.2 HV, the highest density of 94.7 % and the lowest wear rate of 0.00397 $mm^3/m$ were obtained at a milling speed of 720 rpm, a compaction pressure of 794.4 MPa and sintering at 1400 °C in an argon atmosphere. Compared to commercial SS316 and fabricated SS316L, the composites had 7.4 times and 11 times lower wear rate, respectively. However, it is shown that using better densification methods such as hot isostatic pressing (HIP) or hot pressing can further substantial enhanced densification and improve of the composites wear resistance.

Similar to its effects of the strength and the toughness, the remaining porosity was found to substantially affect the wear resistance of the sintered composites. Therefore, the porosity

was used to correct the abrasion parameter in the first step of wear model improvement. The porosity represented a further consideration of the microstructure in addition to the reinforcement particle size introduced earlier by Wayne. In a second model improvement step, the test conditions were introduced in the wear resistance calculation. This model allowed the prediction of corrected wear resistance values that are characteristic of the individual test materials and are widely independent of wear test conditions. The coefficient of correlation of the model was 0.91 with respect to Wayne's data and wear test results from this study, and was 0.66 after generalization to a large range of wear data measured on multiple materials tested under varying test conditions. This opens a potential avenue for a model-based assessment of the wear resistance of novel materials as well as changes that can be expected under different wear conditions.

## ACKNOWLEDGEMENTS

I am extremely thankful to the almighty God who blessed me with all the abilities necessary to accomplish my goals. I wish to express my sincere gratitude to my supervisor, Dr. Michel Nganbe for his exceptional supervision, advice, patience and encouragement throughout this study, Rev Fr. Dr. Edwin Omorogbe for his encouragements, and support during my low times, Dr. Natalie Baddour (Departmental Chair) for been a mentor and Dr. Ali Ourdjini for his contributions and support towards this study as well as Professor G.I. Lawal of the University of Lagos, Nigeria.

I wish to say a big thank you for the great assistance and support I received from all the Professors and staff of the Mechanical Engineering Department at the University of Ottawa for providing all the support, especially the machine shop during my study.

I am also thankful to the University of Ottawa, TETFund (Tertiary Education Trust Fund) and the University of Lagos for all the support throughout my studies.

I would love to acknowledge my friends and colleagues Mr. Ali Mansur (Mechanical), Mr. Abdullah Al-Janah (Electronics) and Mr. Erfan Nazi (Mechanical), Rev. Fr. Ben Iheagwara and Ms. Erin Parks for their endless support and contribution.

I also, would like to thank my parents (Mr. and Mrs. Ebakhaye), my brothers (Rev. Fr. Philip and Richard Ebakhaye), sisters (Geraldine Odujole, Margaret Jegede, Tessy Agaiye and Cynthia Innih) and brothers-in-law as well as my family friends for their amazing love, prayers and support.

A special appreciation to my late mother-in-law (Madam M.O. Kuforiji) who always supported, encouraged and always looked forward to the day I was going to graduate but never saw this day, rest in peace grandma, will always love you!!!

Finally, my utmost gratitude and affection goes to my husband (Engr. Fola Kuforiji) alias “oko mi” for always been my best non official co-supervisor and colleague, never tired listening, discussing, offering recommendations and feedbacks towards the improvement of this study, anytime and anywhere “Eshe Oko mi atata” (Thanks my amazing husband)! My awesome and gracious children Pemi (Honey), Demi (Darlyn) and Temi (Sweet heart) for their endless love, prayers and patience enabling me complete my studies,“ am saying a big thank you from the bottom of my heart”.

# TABLE OF CONTENTS

## LIST OF FIGURES

## LIST OF TABLES

## NOMENCLATURE

| | |
|---|---|
| a | Half indentation diagonal from Vickers hardness indentation test |
| $A_s$ | Abrasive grit size |
| AP | Abrasion parameter |
| $Al_2O_3$ | Aluminum oxide |
| AYP | Apparent yield point |
| BSD | Back scattered diffraction |
| BPR | Ball-to-powder weight ratio |
| b | Empirical factor |
| c | Crack length from the Vickers hardness indentation test |
| c/a | Ratio of the crack length to half length of the indentation diagonal |
| CM | Composite materials |
| Co | Cobalt |
| $Cr_3C_2$ | Chromium carbide |
| $D_C$ | Reinforcement particle size |
| $D_{WC}$ | Carbide grain size |
| E | Modulus of elasticity |
| EDX | Energy-dispersive X-ray spectroscopy |
| $E_{(0)}$ | Young's modulus of the fully dense material |
| $E_{(p)}$ | Young's modulus of the experimental material with porosity |
| F | Load |
| HV | Vickers hardness |
| $H_a$ | Hardness of abrasive |

$H_c$ Hardness of composites

$H_s$ Hardness of surface

HIP Hot isostatic pressing

K Wear coefficient

$K_{IC}$ Fracture toughness of material

Kgf. Kilogram force

M Mass

$M_a$ Mass in air

MA Mechanical alloying

Mo Molybdenum

N Number of particles

Ni Nickel

N/s Newton per seconds

OM Optical microscopy

P Porosity

PM Powder metallurgy

PPR Powder-to-Powder weight ratio

Q Volume of material removed per sliding distance

r Coefficient of correlation

R Abrasive wear resistance

$R_C$ Corrected abrasive wear resistance

S Sliding distance

SEM Scanning electron microscopy

| | |
|---|---|
| TiC | Titanium carbide |
| μm | Micrometer |
| V | Velocity |
| $V_L$ | Wear volume loss |
| $V_m$ | Volume fraction of material |
| Vol.% | Volume percent |
| W | Wear rate |
| WC | Tungsten carbide |
| $W_C$ | Wear rate of composite |
| $W_M$ | Wear rate of material |
| Wt.% | Weight percent |
| ρ | Density |
| $\rho_c$ | Density of composite |
| $\rho_G$ | Green density |
| $\rho_m$ | Density of matrix |
| $\rho_r$ | Density of reinforcement |
| $\rho_s$ | Sinter density |
| $\rho_{th}$ | Theoretical density of composite |
| $\rho_w$ | Density of water |

# 1 INTRODUCTION

## 1.1 Motivation

Increasing the wear resistance and the lifespan of wear components would contribute to reducing maintenance, wear damage costs and ultimately to increasing the equipment efficiency. Ceramic metal composites are known as excellent candidates to meet this challenge. Therefore, this research focuses on the fabrication and the wear investigation of SS316L-$Al_2O_3$ composites. SS316L and $Al_2O_3$ are widely available and at low cost making them viable for potential industrial use. Moreover, both constituents possess excellent properties as detailed in the introduction.

## 1.2 Research objectives

The specific objectives of the research are:

- To investigate the effects of fabrication process parameters on the microstructure of powder, green and final composites well as on the mechanical properties.
- To evaluate the wear properties of SS316L-$Al_2O_3$ composites and compare them with the commercially available 90WC-Co composites, SS316 and unreinforced lab fabricated SS316L.
- To propose improved model approaches relating the mechanical properties and the microstructure to the wear behaviour of the composites.

## 1.3 Background

Mining and exploration involve rock fragmentation in the form of drilling, cutting, digging, crushing and grinding. Machines, equipment and other devices that are designed or adopted for such activities are subject to harsh wear conditions. They are exposed to direct contact with abrasives that are entrapped between the components during operation resulting in 50 % of components failure by abrasive wear [1]–[4]. Component loading during mining can include heavy abrasion, chemically induced wear, fatigue, impact loading, high local temperature and severe temperature gradients [5]. As a result, machines, pumps and other equipment used in such environment can fail prematurely leading to short lifecycles, increased maintenance and replacement costs in addition to the loss of revenue in downtime [6]. Therefore, mining components must possess high hardness to prevent wear, excellent hot strength to prevent distortion, sufficient toughness to prevent cracking due to impacts and fatigue strength to prevent failure due to vibrations.

WC-Co composites is commonly used as a highly wear resistant material in cutting tools, drilling and mining equipment because of its exceptional combination of strength, hardness and wear resistance [7], [8]. However, its toughness and impact resistance are often limited. Therefore, steel components are generally preferred for heavy wear applications such as mining due to their higher toughness and impact resistance.

Considering the above, stainless steel is chosen as matrix for the investigated composites due to its excellent corrosion resistance, high impact resistance and high strength [9]. Aluminum oxide is chosen as hardening particles due to its low cost, chemical inertness, resistance to abrasion and thermal stability [10] during manufacturing.

The present work will focus on investigating the fabrication process; microstructure and mechanical properties of SS316L-$Al_2O_3$ composites for wear applications. The powder metallurgy (PM) processing route will be used since it offers low consumption of energy, high utilization of material as well as dimensional accuracy [5], [11]. PM involves the milling/blending of powder followed by compaction and sintering of the composites. It is very important that the particles are homogenously dispersed to obtain a uniform microstructure [12]. To assess the performance of the fabricated samples, mechanical testing including hardness and wear testing will be performed. Microstructural characterization of the samples will be done using optical microscopy (OM) and scanning electron microscopy (SEM).

## 1.4 Thesis structure

The thesis is structured as follows: The literature review is presented in Chapter 2, the experimental procedure and the employed fabrication processes are described in detail in Chapter 3. Chapter 4 reports the results discussed in Chapter 5 while the conclusions are summarized in Chapter 6. An outline of recommended future work is presented in Chapter 7.

# 2 LITERATURE REVIEW

## 2.1 Powder metallurgy technology and composite materials

Powder metallurgy is the art and science of producing metal powders and the utilization of primarily metal powders for the production of bulk materials and shaped objects [5]. It allows the production of materials that cannot be made through conventional casting processes. Casting difficulties can include reinforcement segregation and clustering, detrimental interfacial chemical reaction, highly localized porosity and poor interfacial bonding which result in deterioration of material properties [13].

Mechanical alloying (MA) is a prominent method for composite powder preparation that allows homogeneously dispersing fine hard particles in a softer matrix [14], [15]. The primary parameters of MA include: the milling time, the milling speed and the ball-to-powder ratio. Fine particles produced by MA show a significant fraction of interface boundaries, a large ratio of interface area-to-volume, and a high degree of disorder of atoms. This results in improvements of the mechanical, chemical and physical properties such as strength, hardness, ductility, toughness, specific heat, diffusivity and excellent tribological properties compared to coarse particle materials made by conventional fabrication processes [16], [17].

The properties of composite materials are influenced by the particle size, the grain size, the dimensionality of systems, the alloying elements, the atomic structure, porosity and other defects. Improved properties of composite materials are primarily based on efficient impediment of dislocation motion. Barriers to dislocation motion can include fine particles, grain boundaries and solute atoms, which increase material's hardness and strength.

Particularly for materials with small grain size, grain boundaries can become a major obstacle to dislocation movement [12].

Lately, powder metallurgy (PM) stainless steel components have been largely used for automotive and structural applications and are becoming more important in high technological areas [5], [18] because of their higher stiffness, strength and toughness compared to aluminum [9], [19]. Powder metallurgy can be used to produce finished or semi-finished products by blending or mechanical alloying, powder compaction and sintering. PM offers advantages such as lower processing temperature below the melting point, near net shape, high final density, greater material utilization and a more refined microstructure with superior material properties as compared to the conventional casting techniques [9], [20]–[22].

Powder metallurgy is an attractive processing route for steel matrix composites because the distribution of the reinforcement is more uniform [9]. It has some limitations including relatively high costs for simple materials and shapes as well as potential hazards during powder handling. However, it allows the flexibility of tailoring the microstructure and properties, and has been proven effective in fabricating high strength and wear resistant powder metallurgy stainless steel through particulate dispersion [23]. Among various grades of PM stainless steels, the austenitic grades are the most widely used with 316L based alloys alone accounting for more than one-third of existing PM stainless steels [6], [14]. Steel matrix composites have been proposed for use as replacement for more costly cemented carbides [9]. The components made of SS316L powder have good mechanical strength, wear and corrosion resistance [18].

### 2.1.1 Mechanical alloying

Mechanical alloying (MA) is one of the most effective modern approaches used in the production of dispersion-strengthened composite materials (CM). The advantage of MA is its flexibility to produce materials with a microstructure that is often impossible to obtain by conventional casting methods. However, a major limitation that impedes the widespread use of MA is the considerable cost of production [11], [24], [25]. During mechanical alloying the kinetic energy of a milling medium is converted into mechanical work in the powder. Due to its special attributes, this simple and effective technique has been applied to metals, ceramics, polymers and composite materials. Particularly, it enables production of a fine dispersion of second phases (usually oxide particles), extension of solid solubility limits, refinement of grain size, blend of novel crystalline and quasicrystalline phases, development of amorphous (glassy) phases, disordering of ordered intermetallics, alloying of difficult to alloy elements, inducement of chemical (displacement) reactions at low temperatures, scalability of the process [15], [26], [27].

Several researchers have used MA to produce ceramic-metal composites with distinct properties. This is because the microstructure can easily be altered to produce different properties for various applications through dispersion strengthening by embedding a reinforcing phase into the matrix. This leads to properties improvement as compared to mixing or blending of the constituents [28]. Final ball milled powders usually have a high surface area-to-volume ratio, enhanced diffusion rates due to a reduction in particle size during the milling process as the initial constituents are subjected to fracturing, deformation and welding.

MA is a complicated process and hence requires the optimization of a number of

variables or parameters to attain the desired microstructure and properties. The effects of parameters such as type of mill, type and size of the grinding medium, ball-to-powder weight ratio, milling time, milling speed or rate, milling aids, milling atmosphere and energy input have been studied. However, these parameters are not completely independent of one another. For example, the optimum milling time is dependent on the type of mill, size of the grinding medium, temperature of milling, ball-to-powder ratio, etc.

During the initial stages of milling, ductile metal powder particles plastically deform upon ball to powder collision while the brittle oxide particles get fragmented as shown in Figure 2.1.

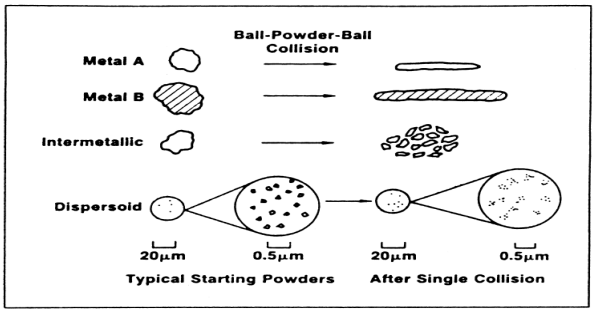


**Figure 2.1: Deformation, fracturing and alloying of powders during mechanical alloying [13].**

These fragmented brittle particles tend to become obstructed by the ductile constituents. With further milling, the ductile powder particles become work hardened; the lamellae become elongated and refined; the lamellae spacing decreases and the brittle particles get uniformly dispersed if they are not soluble in the ductile matrix. On the other hand, if the brittle phase is soluble, alloying occurs between ductile and brittle constituents. However, alloying will also depend on the solid solubility of the brittle material in the ductile matrix.

Sometimes, metal powders are milled in a liquid medium and this is referred to as wet milling. If no liquid is involved, it is referred to as dry milling. Cryomilling is wet grinding with the liquid used at cryogenic temperatures. It has been reported that wet milling is more suitable than dry milling to obtain finer ground materials because the solvent molecules are absorbed on the newly formed surfaces of the particles lowering their surface energy. It has also been reported that the rate of amorphization is faster during wet milling than during dry milling. However, the disadvantage of wet milling is the increased contamination of the powder [14].

### 2.1.2 Powder compaction

The compaction of powder is an important stage in the powder metallurgy process. The green density (density of compressed powder) has a great effect on the final composite [29]. The governing mechanism of the powder compaction process initially starts with rotary rearrangement or restacking processes of the particles. This leads to the collapsing of bridges and the filling of cavities, thereby enhancing the density of the powder. Thereafter, there is an increase of the particle-to-particle contact due to plastic deformation enhancing the green strength and shaping it into the desired geometry of the die cavity. The particles are flattened, oxide films are broken up, powder aggregates are built by mechanical interlocking, and particles become cold-welded [30], [31].

In general, the green density is increased with increasing compaction pressure as reported by several authors [30]–[33]. Simply stated, the role of the compaction pressure is to compress powder particles into a shape, increase the density, and provide strength to the compact [34]. However, increasing green density by compaction has its limitations; beyond a maximum compaction pressure value, only negligible increase in green density can be

obtained [29] and the green compact starts cracking resulting in a reduction of its green strength. Eventually, adhesion between the particles is enforced with further growing of contact surfaces. Methods used for compaction include uniaxial pressing, extrusion, shaping and hot isostatic pressing (HIP) [33], [35]. During HIP the powder is filled into a capsule, which is placed into a heatable pressure tank. The powder is then compacted under a high pressure and simultaneously sintered close to the melting point of the lower melting constituent. The uniaxial powder compaction is probably the most economical and commonly used method. The three stages of the compaction cycle are the filling of the die cavity, the powder compaction and the ejection of the green compact [34], [36].

### 2.1.3 Sintering

Sintering is defined as a thermal treatment for the bonding of particles into a coherent, predominantly solid structure via diffusion that occurs at the atomic scale [37]. When no external pressure is exerted, the process is known as pressureless sintering. Pressureless sintering is an inexpensive consolidation method that can produce a wide range of sintered geometries. However, without external pressure there is no restriction on the deformation of the specimen during sintering, which can lead to severe differences in shrinkage. Despite this challenge, pressureless sintering in a high temperature furnace provides a simple consolidation method well suited for the bulk manufacturing of multiple products. Sinter bonding tends to be temperature sensitive. As the sintering temperature is increased, sintering kinetics generally accelerate. Particle cohesion increases as the porous interfaces between particles are consumed to enhance diffusion between the powder particles in order to achieve grain coalescence. Grain and pore size and shape change during sintering. The initial particle size also has a significant role in sintering kinetics. Important

sinter parameters include sintering temperature, time, atmosphere, additives (compounds mixed with the powder in small quantities), as well as the cooling technique of the sintered product.

#### 2.1.3.1 Sintering temperature

The sintering temperature is significant to the final composite properties. It classifies the type of sintering for a particular material into solid state sintering, liquid phase sintering, super-solidus sintering, etc. During sintering, high temperature causes particle-to-particle diffusion with the formation of grain boundaries and the closing of voids. In most cases, PM stainless steels are consolidated through solid-state sintering at temperatures ranging from 1100 °C to 1350 °C [38]–[42], whereby the compacts are sintered at temperatures below the melting points and the densification of the compact is controlled by solid diffusion [5]. However, sintered materials do have residual porosity, which limits their application.

Several chemical reactions may occur during sintering and a considerable mass transport takes place between particles via the weld bounds. These weld bounds are developed as cohesive necks grow at the points of contact. This means, sintering is a spontaneous process and the difference in free energy between initial (unsintered compact) and final state (sintered compact) is its driving force, as the sintered particles tend to coalesce together minimizing their surface energy. At lower sintering temperatures, densification enhancement can be obtained by using sintering aids that can form a liquid phase.

#### 2.1.3.2 Sintering aid

Sintering is not always a solid-state process, it can also be provided in the presence of a liquid phase. In some cases, especially in the sintering of ceramics, certain additives with low melting point and good wettability are added to the powder. At the sintering temperature, these additives melt and form a thin film of liquid between solid particles to be sintered. The presence of a small amount of liquid phase improves diffusion rates during sintering and stabilizes the desirable crystal structures. This type of sintering is known as liquid-phase sintering, during which both liquid and solid coexist as a result of chemical reaction, partial melting or eutectic liquid formation. Despite densification enhancement however, additives can result in poor mechanical properties, as they tend to segregate at inter-granular regions to form brittle phases.

#### 2.1.3.3 Sintering time

In sintering, densification changes with sintering time during the three stages of sintering:

- Rearrangement: melt flow and penetration repacking, rapid densification, particle sliding.
- Solution-reprecipitation: diffusion controlled densification takes place in areas where the capillary pressures are high, the atoms going into solution favorably and forming precipitates in areas where the chemical potential is lower. That is, where the particles are not close or in contact. This can be accompanied by shape accommodation, grain growth, and neck formation.
- Solid state: This is the final densification stage accompanied with rigid structure neck growth, grain growth, coalescence, and pore coarsening.

The effect of sintering time on densification of different material compacts is similar. For a given temperature, a corresponding sintering time is required for the three sintering stages to be completed [8]. It must be pointed out that too long sintering time can lead to grain growth. In various studies on particle size and sintering atmosphere, it has been shown that finer particle size and higher hydrogen content in the atmosphere lead to faster sintering rate and better densification [38].

#### 2.1.3.4 Chemical composition and particle size of materials

The compositional variation and particle size of composite materials have an effect on their properties before and after sintering. Poor mechanical properties are often obtained from the solid-state sintering of aluminum oxide and steel composites. Yotkaew et al. recommended that further process optimization be made to improve the mechanical properties of SS316L-$Al_2O_3$ composites by super-solidus sintering and mechanical milling of the powder [43]. Also, they noted that the increase in aluminum oxide particle content in SS316L could reduce the sinter density, the tensile strength, the yield strength and the ductility of the composite, which was attributed to sintering prohibition by $Al_2O_3$ particle aggregates. This might be improved by enhancing the wettability of SS316L on $Al_2O_3$ particles.

#### 2.1.3.5 Sintering atmosphere

The sintering atmosphere is a critical parameter to consider during the sintering process in order to avoid unwanted chemical reactions. Some sintering processes prove their effectiveness with pure gases or custom mixtures. In some cases, air is used as working or sintering atmosphere. For most composites however, sintering is done in vacuum or inert gas

such as argon or nitrogen to avoid the presence of oxygen and oxidation. The use of inert gases also reduces contamination levels. The most commercially used sintering atmosphere for stainless steel is the dissociated ammonia, which is made up of 75 vol.% of hydrogen and 25 vol.% of nitrogen in composition. However, nitrogen based atmosphere with composition between 5 vol.% and 10 vol.% of hydrogen can be used in some cases [44]. Pure hydrogen atmosphere can be used, but it is not readily used in industrial scale, as this is very expensive and not cost effective. The major or principal alternatives to dissociated ammonia are the vacuum and argon. Vacuum tends to conserve more energy and is more ecological [44] compared to the use of gases or chemicals. On the other hand, argon atmosphere is low cost and easier to maintain as well as control than vacuum. In this study, the sintering will be done in argon and air atmosphere.

## 2.2 Wear

The wear of materials is a major and widely recognized industrial problem in engineering applications [45]. The direct cost of wear failures includes wear part failures and replacements, increased work and time, loss of productivity, as well as indirect losses of energy and increased environmental burden. Improving the wear resistance will go a long way in lowering excavation and production costs, increasing work efficiency and in reducing operational downtime [6]. For wear resistant components, materials with higher hardness and toughness are required such as high strength steels, high strength low alloy steels, refractory metals, and refractory ceramics. For most wear applications, high-speed steel and cemented carbides are used in most types of wear conditions. Heavy wear components can undergo fatigue; impact loading and abrasive wear during operation.

### 2.2.1 Types of wear

In the exploration and mining industries, components such as jaw crashers and cone crushers undergo heavy wear during operation. Types of wear include abrasive wear, erosive wear, fretting wear, fatigue wear and adhesive wear. If wear problems are not treated in due time, then huge operational costs and losses can be incurred in downtime as it will lead to structural changes, plastic deformation and surface cracking of the component. Different wear mechanisms can occur depending on the lubrication, nature of surfaces, chemical environment and operation conditions. Predominantly for most mining or exploration equipment, the erosive and abrasive wear is of great concern due to its destructive nature and high rate of occurrence (over 50 % of total wear failure) [46]–[48]. Erosive and abrasive wear is produced by loose hard particles. In studying the wear behavior of materials, a distinct mechanism of material removal may be predominant, but several wear mechanism generally operate at the same time [49].

#### 2.2.1.1 Adhesive wear

Adhesive wear is a wear mechanism with the removal of material caused by adhesive forces [50]. It occurs when two solid surfaces in contact are in relative motion [2], leading to the transfer of material between the two solid surfaces or loss of material from either of the surfaces. If the strength of the soft material is less than the adhesive force, the relative motion will deface the soft material, and results in a huge amount of plastic deformation occurring in the contact region producing some wear particles or asperities. Further sliding action causes the asperities on the two surfaces of the materials to adhere or push onto each other. If the contact area between the two asperities is small, the stress around the surface can be sufficiently high to deform the asperities in contact and weld them together, especial

when the temperature around the contact area increases [2]. If the weld strength is greater than the shear strength of the soft asperity material, the soft asperity will be cut by the shear stress and removed from the surface of the soft material. There are several factors that affect adhesive wear: the materials compatibility, the grain size and the lubrication [2], [51].

- Materials compatibility: The similarity between the physical and mechanical properties of both materials is termed their compatibility. The more similar the materials are, the higher their compatibility. Mostly, materials with high compatibility level are more soluble in each other. Therefore, the likelihood of readily forming more atomic bond is high leading to high adhesive wear. However, some metals with low mutual solubility may also have strong adhesion as a result of their electronic structure. For example, transition metals with a d band that is not filled usually bond in the d bands that aren't filled to form strong bonds [2], [51].
- Grain size: The microstructure involves the grain size of the material. According to Hall Petch, the finer the grain size, the higher the material yield strength, and therefore, the greater the material resistance to shear during relative motion [2].
- Lubrication: When the wear surface is lubricated, the contact between surfaces in relative motion is reduced and it is difficult for atomic bonds to form between the surfaces [2], [51].

#### 2.2.1.2 Fatigue wear

Fatigue wear is a material removal as a result of repeated or cyclic stress, giving rise to deformation of the material subsurface in contact with the grits during operation or sliding action. Failure occurs due to repeated deformation of the asperities of the rubbing bodies in contact. At the subsurface, there is usually a high shear stress, which can cause the initiation

and propagation of micro cracks through the material, especially if there are inclusions in this high stress areas. These micro cracks form an isolation when they reach the surface of the material resulting in the detachment of a material lump forming wear particles. Fatigue wear is often affected by the presence of defects in materials such as incoherent inclusions as the stress concentration might be high enough to initiate micro cracking and surface material removal. High hardness, which usually corresponds to a high fatigue resistance, and a smooth surface finish (surface treatment) can improve the fatigue life as well as diminish stress raisers, thereby enhancing surface fatigue resistance as this results in fewer chances to initiate micro cracking [52].

#### 2.2.1.3 Fretting wear

This type of wear is common when two contacting components undergo relative oscillatory motion of very small amplitudes (100 μm - 250 μm). It is usually combinations of several wear mechanism, including adhesive and abrasive wear. Eventually when the wear particles are oxidized, the three-body abrasive wear mechanism can be initiated [51].

#### 2.2.1.4 Erosive wear

Erosive wear is surface damage produced by hard particles in a fluid that strike the surface. It could also be caused by impingement of particles (solid, liquid or gaseous), which remove fragments of materials from the surface due to momentum effect. There are three types of erosive wear [53].

Solid particle erosion is caused by particles in a gas or fluid, liquid drop erosion, cavitation erosion where the fluid becomes unstable and bubbles up, thereby causing degradation on the surface of the solid; and erosion-corrosion that is caused by low-stress

scratching abrasion in a corrosive environment. The behavior of engineering materials to the impingement of the solid particle changes significantly depending on the type of material, material properties and environmental parameters related with erosion wear such as impact velocity, impact angle, hardness, shape and geometry of the particles.

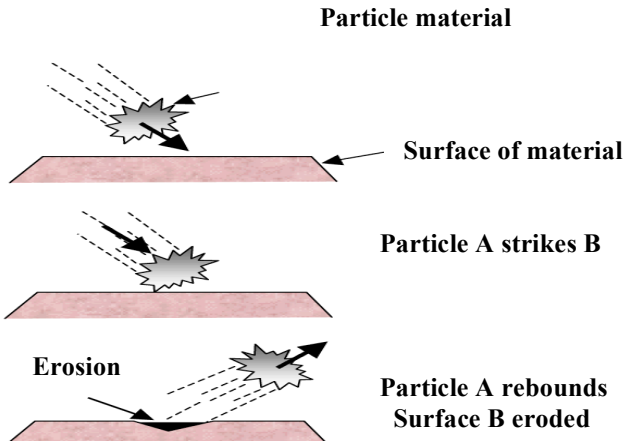


**Figure 2.2: Wear produced by hard particles strike to a flat surface [53].**

Figure 2.2 shows erosive wear produced by solid particle A, striking a solid surface B, which results in the removal of material from the solid surface B.

#### 2.2.1.5 Abrasive wear

Abrasive wear is classified as the removal of material from a surface by loose hard particles sliding between two surfaces [53] and also wear due to particle or protuberances forced against and moving along a solid particle. In machinery, wear occurs most frequently as an abrasive process. It is a common wear type related to earthmoving, mining and minerals processing equipment. Mechanism of abrasive wear include:

- Ploughing: This mechanism is typically governed by plastic deformation. The material is shifted to the sides away from the wear particles resulting in the

formation of a wear groove. The material is not removed from the surface.

- Cutting: This is also governed by plastic deformation. The abrasive particles act as a cutting tool and a chip forms in front of the cutting edge of the particle. The material removed (lost) from the surface has the same volume as the volume of the wear track (groove).

- Cracking: The material cracks in the surface regions surrounding the wear groove when highly concentrated stresses are imposed by the abrasive particles. The volume of the lost material is higher than the volume of the wear track when considering the physical interaction between abrasive particles and surface material as a result of a poor plastic deformation ability of the considered material. Therefore, large wear fragments are removed from the wearing surface owing to micro-crack formation and propagation.

The first two mechanisms are the results of ductile material behavior, while cracking is typical for brittle material behavior. Abrasive wear is usually subdivided into the following classes:

- Gouging abrasion (the removal of large volumes of material per event from the wear surface). The stresses are high at the contact points, but low on the remaining surface similar to a shovel digging into a rock pile.

- High-stress grinding abrasion (the abrasive particle is crushed during the wear interaction). It normally occurs under a low load and high local stress. The wear situation is influenced by two main factors [54]. The properties of the abrasive

particles and those of the material.

- Low-stress scratching abrasion (the abrasive particle remains intact as it moves freely across the wear surface). The stress induced in the abrasion is primarily from the velocity, which is not enough to cause much fragmentation of the abrasive [54].

Abrasive wear depends on material properties like grain size, abrasive particle size, binder content, hardness, fracture toughness and properties of the counter body [55].

The way the abrasives pass over the worn surface determines the type of abrasive wear:

a) Two-body abrasive wear is caused by a hard protuberance on the counter face or hard particles embedded into the counter face. The hard abrasives pass over the surface like a cutting tool and are held rigidly [56] as shown in Figure 2.3. Examples in mechanical operations are grinding such as the action of sand on a surface, cutting and machining.

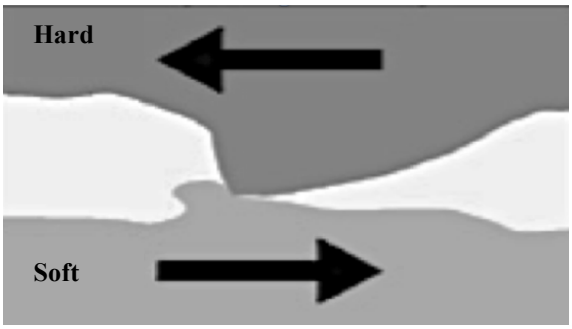


**Figure 2.3: Illustration of two-body abrasive wear [53].**

b) Three-body abrasive wear is caused by small particles or abrasives that are free to roll or slide between the contact surfaces since they are not held rigidly as shown in Figure 2.4. The loose abrasive particles are mostly trapped between the rolling or sliding surfaces and often indent and settle into the softer surface. Wear of bearings

is one example when the grits are trapped at the interface of the bearing.

It is important to know the properties of the abrasive particles to understand what kind of damage they can produce. The hardness of the abrasive particles can influence the rate of material removal from the surface.

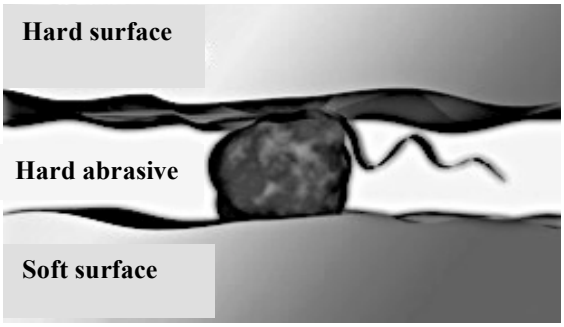


**Figure 2.4: Illustration of three-body abrasive wear [53].**

Abrasive particles ($H_a$) must have higher hardness than the hardness of the surface ($H_s$) to be able to scratch it. The rate of material removal decreases significantly when the hardness of the surface approaches the hardness of the abrasive. The wear rate is much more sensitive when $H_a/H_s$ is less than ≈1 [57]–[59]. Depending on the hardness of the abrasive ($H_a$), the following damages can occur during operation:

a) If $H_a/H_s > 1.2$, plastic indentation is produced on the surface. This is known as hard abrasion [60].

b) If $H_a/H_s < 1.2$, there is no plastic indentation produced on the surface. This is known as soft abrasion [60], which exhibits a lower wear rate [61], [62] or material loss.

#### 2.2.1.5.1 Abrasive wear testing

Abrasive wear can be tested using different methods including the pin-on-disc test. Hereby, a pin shaped sample fixed on an arm is pressed under a constant load against an abrasive disk or a rotating wheel, and is made to slide against a pin sample with loose abrasive particles continuously fed between the abrasive disk and the pin during the testing process [63], [64] as shown in Figure 2.5.

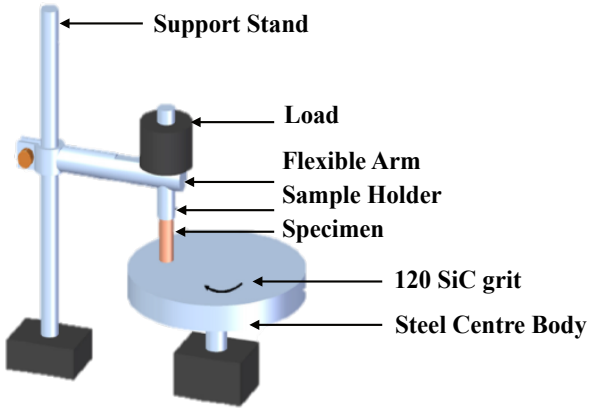


**Figure 2.5: Schematic illustration of the pin-on-disk wear tester [63].**

The material removal is usually measured by weighing the sample before and after each wear test. The wear rate varies with factors such as the load applied, the type of abrasive disk, the rotating speed of the disk and the sample or specimen material.

## 2.3 Characteristics of wear components

Mining wear components are often subjected to heavy abrasion, chemically induced wear, fatigue and impact loading during operation. Therefore, wear components must be designed to have sufficient toughness in order to withstand high impacts to minimize crack initiation and propagation. In addition, excellent hot strength and thermal stability are

required to prevent plastic deformation at high temperature during operation, high hardness to reduce indentation; as well as fatigue strength to prolong the durability or lifespan of the component.

### 2.3.1 Hardness

Hardness is a critical parameter influencing wear resistance. It is a parameter describing the material's resistance to indentation, scratch and deformation by means such as abrasion, drilling, impact, scratching or wear. Increased hardness results in increased wear resistance, reduced wear rate and prolonged lifespan [6]. The hardness of ceramic-metal composites is mainly improved or enhanced by increasing the ceramic content. Imbaby et al. [65] and several other researchers have reported great increase in the hardness of alumina-stainless steel composites, as the volume content of $Al_2O_3$ (ceramic phase) is increased [38], [43], [65]–[67]. However, as the hardness is increased, the toughness is decreased leading to brittleness. Therefore, the best combination of hardness and fracture toughness has to be determined in order to achieve an optimum performance.

### 2.3.2 Fracture toughness

Fracture toughness is a measure of the material's resistance to the propagation of cracks. It is used extensively to characterize the fracture resistance of ceramics and composite materials [68]. The fracture toughness may serve as a basis for structural flaw tolerance assessment. Awareness of differences that may exist between laboratory test and field conditions is required to make proper flaw tolerance assessment. Wear can occur by fracture only when a critical load on individual abrasive particles is exceeded [2]. The toughness of composites is highly dependent on the structure of the materials, which

includes the size, amount and distribution of hard particles in the matrix. The sample preparation for the measurement of fracture toughness is usually time consuming and expensive as most of the conventional techniques require very precise notch geometries. Therefore, the fracture toughness is often evaluated using the Vickers hardness indentation method. In this method, the toughness is accessed using cracks created at indentation corners as shown in Figure 2.6.

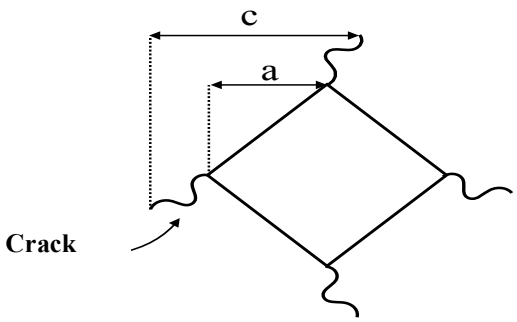


**Figure 2.6: Vickers indentation mark with c: crack length; and a: indent diagonal [68].**

However, various models have been developed for the computation of the fracture toughness by several researchers either using experimental or empirical methods. The fracture toughness measured is often dependent on the micro-indentation hardness of the material, the crack length 'c', the indentation diagonal half-length 'a' and the applied load on the material during Vickers indentation. However, some models require the values of the Young modulus and Poisson ratio [68]. The indentation fracture toughness is computed using the direct crack measurement method. The crack formation often falls into two classes: median or Palmqvist cracks. Palmqvist cracks form under small indentation loads as small cracks at indent corners as seen in Figure 2.7b. At high loads, fully developed median cracks form joining opposite indent corners and running beneath the indent in a half penny shape geometry as seen in Figure 2.7a.

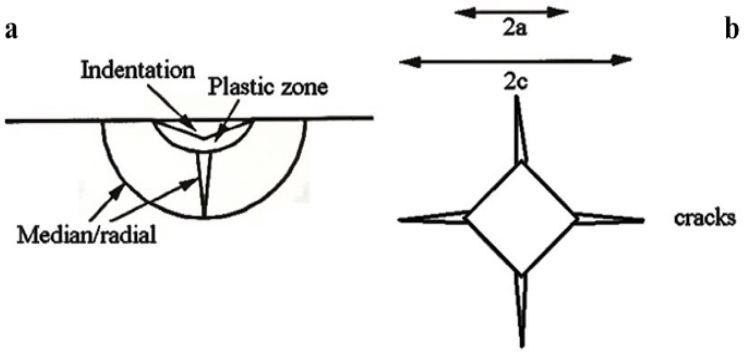


**Figure 2.7: Crack configuration around hardness indentation: (a) Median and radial crack configurations; (b) Measurement of crack length 2c and indent diagonal 2a [68].**

## 2.4 Wear resistance

The combination of hardness and toughness is a very important factor in determining the wear resistance of materials [69]. Wear depends on the resistance of the material to penetration by the abrasive particles during contact or sliding action as well as on the obstruction of plastic flow and fracture. Therefore, increasing hardness and toughness in metallic or ceramic materials improves the wear resistance of components used in wear environments. However, increasing the hardness generally also results in a reduction in toughness. Introducing a secondary phase can enhance the wear resistance [5], [6], [12], [16] of particle-reinforced metal matrix composites.

The abrasive wear resistance can be improved by optimizing the mechanical properties of both the matrix and the reinforcement phase [70]–[72], the microstructure [71], [73], [74], size and volume fraction of the reinforcing phase, as well as the nature of the interface between the matrix and the reinforcement [75]. This can be achieved by controlling the various process parameters during production. Gulsoy et al. observed that an increase in the volume fraction of reinforcement, longer sintering time at 1405 $^{\circ}$C and strong interfacial

bond strength reduced the wear rate of composites [66]. Allen et al. observed in ultra fine grain (0.49 microns) WC-Co hard metals that the wear resistance increased to about twice that of the fine grade (0.81 microns) of WC-Co composite [76].

## 2.5 Abrasive wear modeling

Abrasive wear modeling is a subject of concern that aims at a continuous study in the improvement and the prediction of material removal during operation in applications involving wear. It provides a relationship between wear, design parameters and application. This enables the prediction or estimation of component failures, repairs and maintenance requirements, materials and energy saving, and design optimization. The most widely used model for wear prediction is the Archard's wear equation for abrasive wear because of its simplicity as seen in Equation 2.1.

$$\boldsymbol{Q = \frac{K.F}{HV}} \tag{2.1}$$

Where Q is the volume of material removed from the surface per unit sliding surface; F is the normal load applied; HV is the hardness of the material; and K is the coefficient of wear [4], [77], [78].

Khrushov and Babiched related the wear resistance of composites to that of their constituent phases using the inverse rule of mixture as in Equation 2.2. The approach is based on the assumption that the constituents of the composites wear at an equal rate during operation.

$$\boldsymbol{R = \sum_{i=1}^{m} \frac{1}{W_i} = \sum(\frac{V_1}{W_1} + \frac{V_2}{W_2} + \cdots + \frac{V_m}{W_m})} \tag{2.2}$$

Where R is the wear resistance; W is the wear rate; V is the volume fraction; and the indices 1 and 2 represent phase 1 and phase 2, respectively. However, it is often recognized that primarily the wear behavior of most composites is strongly determined by the volume fraction of the reinforcement [75], [79]–[81].

Zum-Gahr et al. developed a second wear equation for multiphase materials in order to explain experimental data. The approach is known as the linear rule of mixture. They argued that the wear behavior of a multiphase material is not dominated by a single phase, but rather that the contribution of each individual constituent is linearly proportional to its volume fraction in the composite as described in Equation 2.3 [75], [81].

$$\boldsymbol{W = \sum_{i=1}^{m} V_i W_i = \sum (V_1 W_1 + V_2 W_2 + \cdots + V_m W_m)} \tag{2.3}$$

Evans and Marshall [82], [83] proposed a model based on lateral cracking in the material considering all particles involved. The number of particles N was calculated as the cross sectional area of the sample divided by the diameter of the particle. The volume loss per unit sliding distance Q was given by;

$$\boldsymbol{Q = \alpha_3 N \frac{(E/_{HV})\, F^{9/8}}{K_{IC}^{1/2}\, HV^{5/8}}} \tag{2.4}$$

Where $\alpha_3$ is a material independent constant; N is the number of particles each carrying the load F; E is the modulus of elasticity; $K_{IC}$ is the fracture toughness; and HV is the hardness of the worn material. In another approach, the volume loss per sliding distance Q is written as in Equation 2.4 [84].

$$\boldsymbol{Q = K\ \frac{F^{5/4}}{K_{IC}^{3/4} HV^{1/2}}} \tag{2.5}$$

Where K is a constant known as the abrasion wear resistance coefficient.

Equation 2.5 suggests that the material wear depends stronger on the toughness (raised to the power of ¾) than on the hardness (raised to the power of ½). The different exponents in Equation 2.5 are determined semi empirically and may vary with respect to different models or materials [2].

Wayne et al. [85], [86] observed from previous work that the abrasion wear resistance of a material cannot be based on its mechanical property alone. Therefore, he proposed Equation 2.6 that includes the grain size as microstructural parameter.

$$\boldsymbol{R = K\frac{K_{IC}^{3/8}\ HV^{1/2}}{D_{WC}}} \tag{2.6}$$

Where R is the abrasion resistance; $K_{IC}$ is the fracture toughness; HV is the hardness; and $D_{WC}$ is the carbide grain size. For brittle ceramics where there is no ductile phase to prevent large scale brittle fracture, a higher dependence on the fracture toughness and a correspondingly lower dependence on the hardness were observed [87] as in Equation 2.7.

$$\boldsymbol{R \propto K_{IC}^{3/4}\ HV^{1/2}} \tag{2.7}$$

Bodhak et al. [88] suggested the abrasive model in Equation 2.8 for cases where abrasive wear is controlled by substantial plastic deformation accompanied by ceramic particle fracture.

$$V_L \propto \frac{F^{1/8}}{K_{IC}^{1/2} HV^{5/8}} \quad (2.8)$$

Where $V_L$ is the wear volume loss (normalized with respect to the normal load); F is the contact force; $K_{IC}$ is the fracture toughness; and HV is the hardness.

## 2.6 Improving wear resistance in composites

Introducing a secondary phase into a matrix material [4], [75], [89] can enhance its wear resistance. Such a composite then basically consists of a matrix and reinforcement often in the form of particles or fibers, and the interface between the matrix and the reinforcement. The improvement of wear resistance of a composite depends on the morphology, distribution, volume fraction and mechanical properties of the reinforcing phase [2], [64], [90]. Also, the wear resistance can be varied significantly by alteration of the microstructure. The composite properties are defined by the weakest links in their structure. Therefore, the strength of composites also widely depends on the strength of the bond between the reinforcement and the matrix [50]. A strong interfacial bond can transfer and distribute the load efficiently from the matrix to the reinforcement. The lower hardness of metals compared to ceramics leads to relatively rapid material removal during the wear by harder ceramic abrasives. Ceramic materials on the other hand, lack the necessary toughness and the impact resistance required for many mining and oil sands applications. Ceramic-metal composites owe their excellent tribological properties to a combination of high hardness of the ceramic particles along with the toughness of the more ductile metal matrix [6], [91]. However, increasing the hardness mostly results in loss of toughness. Therefore, an optimum combination of hardness and toughness must be achieved. Microstructure refinement has been proven to potentially increase both the hardness and toughness as seen

in Figure 2.8 [92].

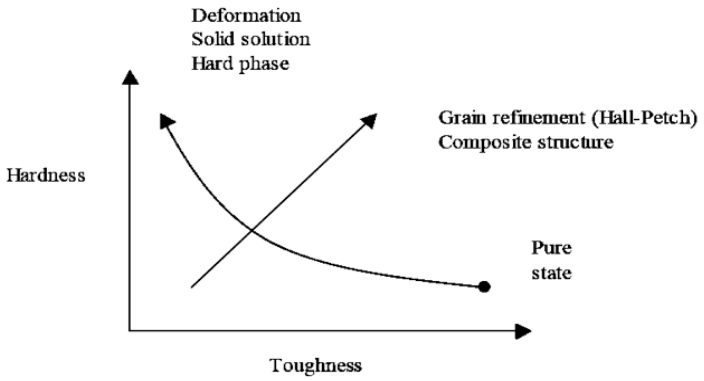


**Figure 2.8: The hardness vs. toughness relationship of metal-based materials** [92]**.**

## 2.7 Current wear resistant materials

### 2.7.1 High strength low alloy steel (HSLA)

HSLA steels or micro-alloyed steels are designed specifically to provide better mechanical properties and/or greater resistance to atmospheric damage than conventional carbon steels. HSLA steels are designed to meet specific mechanical properties such as a yield strength greater than 275 MPa. They are much stronger and tougher than ordinary carbon steels; they are ductile, highly formable, weldable and highly resistant to corrosion. The extra strength of HSLA steels makes them more durable and gives them a longer life span. However, high strength low alloyed steels still have great difficulty in meeting challenges that result in failure of metal parts due to dual effects of wear and oxidation at high temperature. They often fail to simultaneously provide for impact resistance, excellent wear, and sufficient toughness and oxidation resistance. Therefore, they are often inappropriate for heavy wear application. Instead, they are widely used as stationary

structural components and for mobile equipment such as lighting poles, oil storages, automobile components, earth moving and mining equipment [93].

### 2.7.2 WC-Co composites

Tungsten carbide cobalt (WC-Co) hard materials have been widely used for producing cutting, drilling, and forming tools because of their high hardness and relatively high fracture toughness. WC-Co possesses high wear resistance and rupture strength, which makes it a promising material for applications where good wear resistance is required [94]. It provides increased tool lifetime compared to conventional high-speed steel. It is in the class of hard metals known as cemented carbides. The WC grains provide high hardness and wear resistance. However, the main microstructural characteristics that govern the wear behavior are related to the grain size of the WC, the interfacial bonding between the two phases and the volume fraction of the binder [60], [95], [96].

**Table 2.1: Properties of representative grades of cemented carbides [80].**

| Cemented carbide | Room Temp. Hardness HV | Modulus of elasticity GPa | Transverse rupture strength MPa | Coefficient of thermal expansion $10^{-6}$ /K | Thermal conductivity W/m.K | Density g/cm$^3$ |
|---|---|---|---|---|---|---|
| WC-20 wt.%Co | 1050 | 490 | 2850 | 6.4 | 100 | 13.55 |
| WC-10 wt.% Co | 1625 | 580 | 2280 | 5.5 | 110 | 14.50 |
| WC-3 wt.% Co | 1900 | 673 | 1600 | 5.0 | 110 | 15.25 |
| WC10 wt.% Co-22 wt.% (Ti, Ta, Nb)C | 1500 | 510 | 2000 | 6.1 | 40 | 11.40 |

A good combination of these conditions yields optimal properties for wear applications. The properties of sintered WC-Co composites are critically dependent on their final composition and structure [26], [27] as summarized in Table 2.1. Important advantages of WC-Co composites are high hardness, high elastic modulus, high thermal conductivity and low thermal expansion. The limitations of WC-CO composites are that they can deform plastically at high temperatures, they are economically unattractive for some applications and their corrosion resistance is low in an aggressive environment [60]. When plastic deformation occurs, the hard phase breaks down, and the binder phase between the grains slides causing grain boundary slide [53], [97].

### 2.7.3 Aluminum oxide and steel composites

Hard ceramic particles can be incorporated into steel using powder metallurgy to produce metal matrix composites that would otherwise be difficult to produce by conventional methods. Metal matrix composites involving high-speed steels and stainless steel have been studied in recent years. These studies have revealed that the addition of 2.5 to 5 wt.% of $Al_2O_3$ or $Y_2O_3$ and $Al_5Y_3O_{12}$ promotes better corrosion resistance and wear properties in stainless steels [66]. In addition, metal matrices with high strength sustain ceramic particles effectively for improved wear resistance [98], [99]. The choice of alumina comes from the fact that it is very hard with a Vickers hardness of HV=24 GPa [100]. In addition, it possesses good thermal and dimensional stability [101], high thermal expansion coefficient of 8.8 x $10^{-6}$ /$^{o}$ C, high melting point, good chemical inertness, high wear resistance and is low cost [98], [99].

Gulsoy et al. reported that a clean interface free from any diffusion alloying or reaction was obtained when reinforcing SS316L with $Al_2O_3$ particles using hot isostatic

pressing. However, the composites reinforced with the $Al_2O_3$ particles resulted in low wear resistance particularly at high volume fraction [66]. Also, Panda et al. examined the addition of (5 and 10 wt.%) yttria alumina garnet in SS316L and reported no improvement in the mechanical properties and wear resistance in the compacts sintered in microwaves compared to conventional sintering, which was attributed to an elongated irregular pore structure [38]. Tongsri et al. investigated the effect of powder mixture conditions with addition of 2 wt.% $Al_2O_3$ powder particles in SS316L using ball milling and reported a decrease in strength as well as high amount of void or porosity as result of poor distribution of $Al_2O_3$ particles in the composites and poor sintering between both constituents [21].

However, Vardavoulias et al. showed improved wear resistance after 5 wt.% $Al_2O_3$ particle additions in two PM austenitic stainless steels (316L and 304L) using two sintering activators (BN and $B_2Cr$) [67]. Shamsuddin et al. investigated the fabrication of Fe-12Cr-$Al_2O_3$ composites by blending all constituents in a drum for 30 minutes and varying the wt.% of alumina addition in the matrix. They reported that beyond the 20 wt.% addition of alumina, clustering of the reinforcement was observed, which caused a higher porosity and reduction in the density, and hence resulted in a decrease in hardness [102]. Auger et al. investigated the sintering of alumina matrix-stainless steel dispersion composite and the interaction between chromium, carbon, and alumina during the powder metallurgy process. They reported the formation of chromium carbide in some experimental conditions. They observed that samples with 30-50 vol.% steel showed a different behavior compared to others because the remaining carbon content in alumina was observed not high enough for carbide formation in stainless steel, as the carbon is totally absorbed. Therefore, its inhibiting effect does not occur, as there is no formation of chromium carbide. Above 50

vol.% metal fractions, the densification was controlled by stainless steel and was independent of the carbon and chromium contents [103].

Rahimian et al. [104] studied the effect of production parameters on the microstructure and wear resistance of powder metallurgy Al-$Al_2O_3$ composites using ball milling. They varied the particle size of the alumina powder in the aluminum matrix as well as the sintering time and temperature. They reported a decrease in the density with an increase in the wt.% of alumina addition to the matrix, an increase in the hardness and wear resistance as well as the microstructure. They also reported that inappropriate sintering conditions resulted in the deterioration in hardness and a reduction in the wear resistance of the composites. The reduction of the particle size from 48 μm to 3 μm led to a 16 % increase in volume loss. However, the drop in wear resistance was particularly strong in the lower particle size range (from 12 μm to 3 μm) raised the volume loss by a factor of 10 as the particle size decreases into the nano-scale using a AISI4140 steel disc counter surface, a load of 5N, a sliding distance of 1500 m and a velocity of 1 m/s.

Tjong et al. investigated the abrasion resistance of SS304 reinforced with $TiB_2$ hard particles. The composites were fabricated using the isostatic pressing (HIP). The wear test was done using pin-on-disk testing with a 240 grits SiC abrasive disk. They reported an increase in abrasive wear resistance and a decrease in the volume loss of the composite when the $TiB_2$ content increases. The addition of $TiB_2$ to SS304 was found beneficial as it improved the wear resistance of the stainless steel alloy by approximately factor 10 due to the high hardness of the $TiB_2$ particles [62].

### 2.7.4 Research work

In this research, the fabrication, microstructure and mechanical properties of SS316L-$Al_2O_3$ composites are investigated. The two composite constituents are used at an equal ratio of 1 to 1 or 50 wt.% to 50 wt.% in an effort to achieve both sufficient hardness and toughness. The powder metallurgy route is used for fabrication and the wear behavior of the composites is studied under dry sliding wear conditions using pin-on-disk testing. Model correlations are developed considering the microstructure parameters, mechanical properties and wear conditions.

# 3 MATERIALS AND METHODS

## 3.1 Materials and mechanical alloying

Water atomized SS316L powder of irregular shape with 12-44 μm particle sizes and $Al_2O_3$ powder with 10-44 μm particle sizes were purchased from Atlantic Equipment Engineers (AEE) and used as starting materials. $Al_2O_3$ powder was of 99.5 % purity. The chemical composition of SS316L powder is shown in Table 3.1 and the relevant properties of both raw materials are summarized in Table 3.2 as specified in the AEE product chart.

**Table 3.1: Chemical composition of SS316L powder.**

| | C | Ni | Cr | Mo | Mn | $O_2$ | Si | P | S | Fe |
|---|---|---|---|---|---|---|---|---|---|---|
| Wt.% | 0.02 | 11.69 | 16.74 | 2.15 | 0.08 | 0.37 | 0.63 | 0.02 | 0.001 | Balance |

**Table 3.2: Some relevant properties of SS316L and $Al_2O_3$.**

| **Parameters** | **SS316L** | **$Al_2O_3$** |
|---|---|---|
| Melting Point | 1425 $^{\circ}$C | 2072 $^{\circ}$C |
| Density | 7.9 g/cm$^3$ | 3.965 g/cm$^3$ |
| Vickers Hardness | 165 HV | 2285 HV |

The experimental flow process chart is shown in Figure 3.1 using the powder metallurgy fabrication route with SS316L and $Al_2O_3$ as the starting powder constituents.

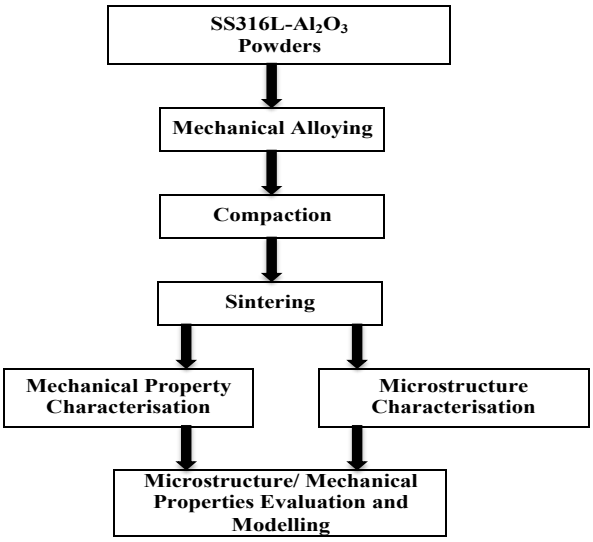


**Figure 3.1: Experimental flow chart of the PM process route.**

SS316L and $Al_2O_3$ powders were used at a weight ratio of 1:1. Ball milling was done using a custom-made attritor mill comprising a stainless steel vial and a rotating shaft. Stainless steel milling balls were used. The ball diameter was 3 mm and the ball-to-powder ratio was 10:1. Ethanol 99 % was used as milling aid and cold tap water was circulated around the vial for cooling. Two shaft-rotating speeds were used for mechanical alloying. SET1 powders were milled at 720 rpm and SET2 powders at 800 rpm. Mechanical alloying was done in cycles of 120 minutes milling and 60 minutes resting periods. Powder samples were taken after every 5 cycles; that is, after every 10 hrs effective milling time. The final milling duration was 30 hrs for SET1 (720 rpm), 20 hrs, 30 hrs and 50 hrs for SET2 (800 rpm). The custom-made attritor mill and the inside of the milling process are shown in Figures 3.2 and 3.3. Two drying methods were investigated: for air-drying (SET1A and B), the powder was spread in a pan and placed in the fume hood for 24 hrs, while for heat-drying (SET1H) the pan was placed on a tabletop heater for 3 minutes at 60 $^{\circ}$C. A

thermocouple was used to monitor the temperature. Table 3.3 highlight the parameters used for the mechanical alloying of the SS316L-$Al_2O_3$ composite powders.

**Table 3.3: Parameters used for mechanical alloying experiments.**

| No. | Constituents | Weight (grams) | Powder-to-powder ratio<br>Ball-to-powder ratio | Time (hrs.) | Speed (rpm.) |
|---|---|---|---|---|---|
| SET1 (A,B,H) | SS 316L | 50 | 1:1 | 30 | 720 |
| SET2A | $Al_2O_3$ | 50 | 10:1 | 20 | 800 |
| SET2B | Balls | 1000 | | 30 | 800 |
| SET2C | | | | 50 | 800 |

**Figure 3.2: Custom-made attritor mill.**

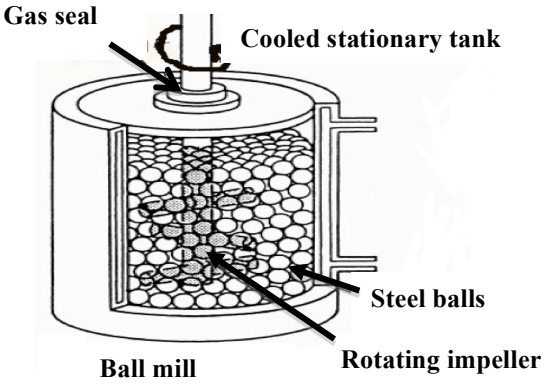


**Figure 3.3: Inside of a milling vial [14].**

## 3.2 Compaction and sintering

The SS316L-$Al_2O_3$ composite powders were uniaxially compacted using a 10 mm diameter die (Figure 3.4). A Rodgers hydraulic press and a custom-made tool steel die were used. Hi-Temp1800 Barium nitride powder mold release was applied to the inner surface of the die to reduce friction, improve compaction and ease sample ejection.

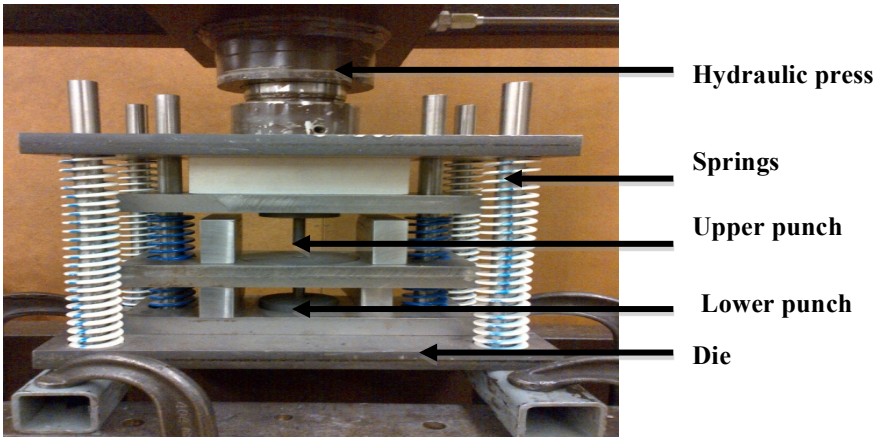


**Figure 3.4: Compaction set-up in hydraulic press.**

The die was then filled up with a desired amount of powder. Uniaxial pressure was applied using the hydraulic press. At the start of the powder compaction, the powder particles are loose and as the pressure is applied they begin to glide over each other without any resistance resulting in the rearrangement of the powder particles.

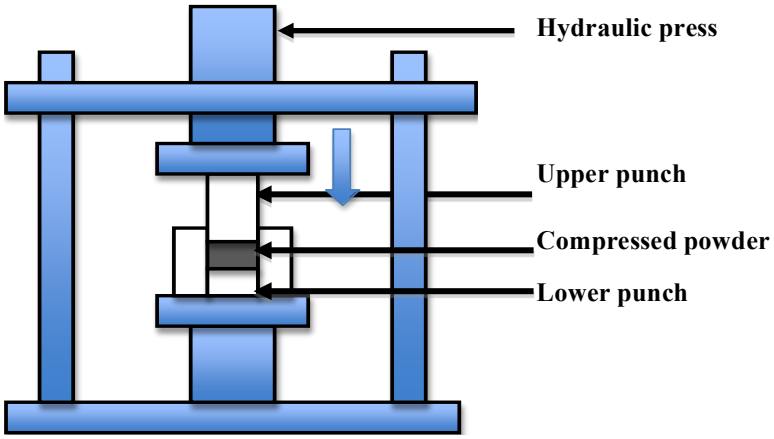


**Figure 3.5: Schematic diagram of a uniaxial compaction set-up [105].**

As the pressure is increased, plastic deformation of the powder takes place as the particles become interconnected. When the desired pressure is reached, the upper punch is

moved back up and the green compact is ejected from the die. Figure 3.5 shows a schematic set-up of a uniaxial compaction die as used in this study.

Different compaction pressures ranging from 595.8 MPa to 1125.4 MPa were used in order to determine the optimum compaction pressure. Four samples were compacted for each compaction pressure and sample type or variant. The compaction displacement was measured using a linear variable differential transformer (LVDT) while the compaction load was measured using a load cell. The green and sinter densities were determined using the Archimedes' principle.

**Table 3.4: Summary of the various manufactured SS316L-$Al_2O_3$ composites.**

| Composites | Wt. $Al_2O_3$ (%) | Milling speed (rpm) | Milling duration (hrs) | Drying method | Sinter holding time (mins) | Sinter temperature (°C) | Sinter atmosphere | Furnace heating rate (°C/min) |
|---|---|---|---|---|---|---|---|---|
| SET1A | 50 | 720 | 30 | Air | 60 | 1150 | Air | 10 |
| SET1H | 50 | 720 | 30 | Heat | 60 | 1150 | Air | 10 |
| SET1B | 50 | 720 | 30 | Air | 60 | 1400 | Argon | 12 |
| SET2A | 50 | 800 | 20 | Air | 60 | 1400 | Argon | 12 |
| SET2B | 50 | 800 | 30 | Air | 60 | 1400 | Argon | 12 |
| SET2C | 50 | 800 | 50 | Air | 60 | 1400 | Argon | 12 |

SET1A and SET1H samples were sintered at 1150 °C in an electric Lindberg furnace in air atmosphere (Figure 3.6a). Slow heating and cooling were used as the samples were left in the furnace during both heating and cooling. All other fabricated samples as seen in Table 3.4 above were sintered in an Oxygon FC700 vacuum furnace (Figure 3.6b) under argon atmosphere. The sintering was performed at a temperature of 1400 °C with a holding time of 60 minutes. A heating rate of 12 °C/min was used and the samples were also furnace heated and cooled.

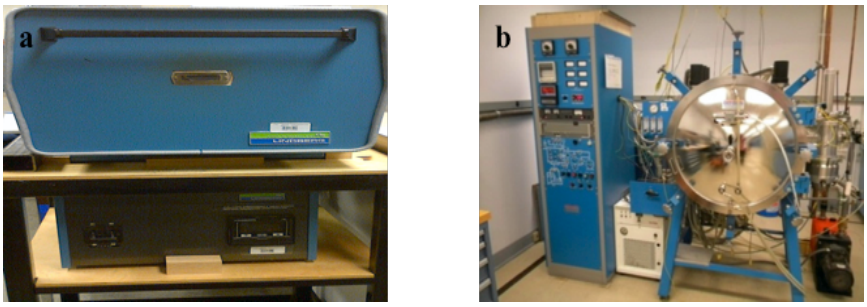


**Figure 3.6: Furnace used for sintering: (a) Lindberg furnace; (b) Oxygon FC700 Vacuum furnace.**

## 3.3 Metallography and hardness testing

Metallographic samples were hot mounted in epoxy resin using a Struers Labopress-3 press. A temperature of 150 $^{\circ}$C and a 20 kN press force were used. The mounted samples were ground and polished using a Struers TegraPol-31 machine and etched using Nital (a solution consisting of 25ml methanol, 25ml HCl and 5ml $HNO_3$). Etching time ranged between 20 and 30s. The microstructures of milled powder, green compacts and sintered samples were characterized using optical (CLEMEX) and scanning electron microscopy (CARL ZEISS).

**Figure 3.7: Clemex optical microscope (OM).**

The Clemex Vision-Lite Version 5.0 image analysis software was used for quantitative microstructure characterization as seen in Figure 3.7. Powder characterization allowed the study of the milling process and its progression. The analysis of the green compacts and sintered samples allowed assessing the homogeneity of phases, porosity and microstructure.

Scanning electron microscopy (SEM) was used for the investigation of the alumina particle structure, homogeneity and distribution employing both secondary electron (SE) and back scattered electron (BSE) imaging to study the morphology. Also, energy dispersive x-ray (EDX) analysis was done for qualitative compositional analysis on some samples as shown in Figure 3.8. The SEM samples were cleaned with ethanol and blown to dry using compressed air to remove any dust particles on the surfaces. The samples were gold coated in a sputtering coater vacuum chamber. The gold platted samples were mounted on a metal stub with adhesive tape and a copper tape is placed from the top surface of the sample to the holder.

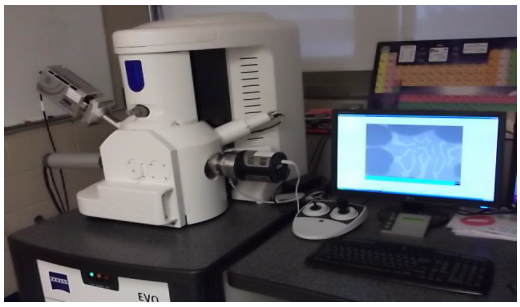

**Figure 3.8: ZEISS Scanning electron microscope (SEM).**

The porosity level of the green and sintered compacts was measured on the SE/BSE micrographs at various magnifications up to 2000X using the Clemex Vision-Lite, Version

5.0 image analysis software. The average values were attained from eight (8) images for each fabricated sample.

The Buehler Wilson hardness micromet 6030 tester (Figure 3.9) was used to measure the Vickers hardness at a load of 500 grams and a dwelling time of 10 secs. The micro hardness was measured on green (compacted) and sintered samples. Approximately 15 micro hardness readings were taken on each sample to determine average values and standard deviations.

**Figure 3.9: Buehler Wilson hardness micromet 6030 tester.**

## 3.4 Volume fraction of phases and $Al_2O_3$ grain size analysis

The phase volume fractions were analyzed using image analysis. The constituents and the reinforcement grain sizes were estimated from SEM/BSD images using the line intercept method on high magnification micrographs. A set of lines was drawn in a systematic sequence across the micrographs of the powder composites and the lengths of all alumina intercepts were measured in order to avoid biased measurements.

### 3.5 Porosity measurement

The porosity of the fabricated composites was determined using image analysis. The SEM and BSD images taken from polished samples and the image J software were used. For each sample, six (6) images were used to calculate the average pore volume fraction.

### 3.6 Fracture toughness measurement

The fracture toughness of the SS316L-$Al_2O_3$ composites was assessed by the indentation method. The Vickers indentation fracture toughness measurements were done on the sintered samples using a load of 5 kgf. The length of indent cracks was measured using the Clemex optical microscope with the lite vision 5 image software, at magnifications between 100 to 400 using 10 indentations for each material state. The indent diagonal half-length (a) and the crack half-length (c) measured from the centre of the indent were used for the calculation of the fracture toughness. The fracture toughness ($K_{IC}$) was calculated using the Palmqvist equation [106], [107] that applies to c/a ratio below 2.5 [108] which was found to be the case for the investigated composites.

$$\boldsymbol{K_{IC} = 0.079 \left(\frac{F}{a^{3/2}}\right) \log\left(4.5 \frac{a}{c}\right)} \tag{3.1}$$

Where F is the indentation load, c is the crack length from the centre of the indent to the crack tip; and a is the indentation half diagonal.

### 3.7 Abrasive wear testing

Abrasive wear tests were performed using a custom-made pin-on-disc tribometer as shown in Figure 3.10 according to the ASTM G132 standard. The samples for the wear testing were cylindrical with a diameter of 8.5 mm and a height of 13 mm. The

samples were grounded and polished with a 3 μm dia pro MD mol suspension prior to testing. A P120 grit silicon carbide (SiC) grinding paper was used as the counter-face. The samples were cleaned with ethanol and dried prior to weighing. Weighing was done at intervals of 300 meters at the end of each wear test using a digital Sartorius electronic scale with 0.1 mg accuracy.

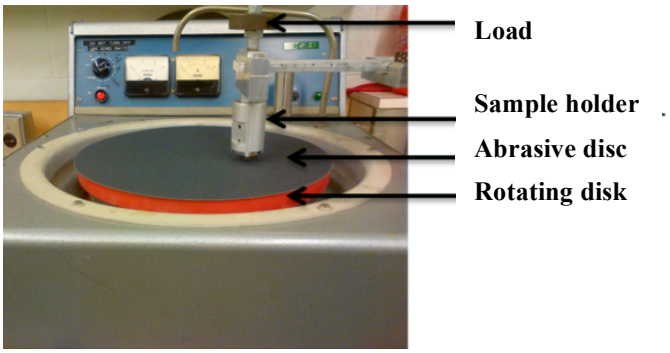


**Figure 3.10: Photograph of the pin-on-disk wear test set-up.**

Dry sliding experiments were carried out under a normal load of 2 N at a sliding velocity of 1 m/s. A new abrasive paper was used for each test sample. The mass loss was recorded for a total track length of 3000 meters attained at an effective duration of approximately 50 minutes for each sample. Four wear tests were conducted for each material under identical conditions for averaging. Figure 3.11 shows the wear track of the different fabricated samples during the wear testing on the SiC abrasive disk under same testing conditions. This shows the virtual examination of material removal of the unreinforced SS316L, the commercial SS316, SET1B and the SET2A composites.

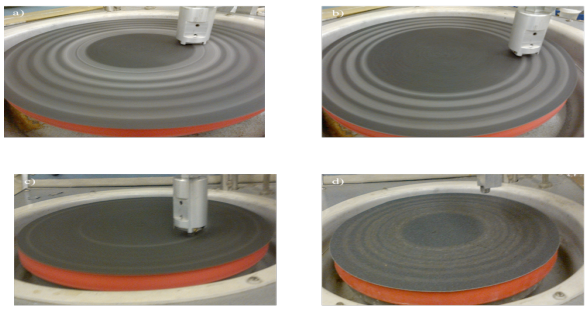

**Figure 3.11: Counter-face of wear track of materials with deposited debris: (a) fabricated SS316L; (b) commercial SS316; (c) 720 rpm for 30 hrs (SET1B) composites; (d) 800 rpm for 20 hrs (SET2A) composites.**

Abrasive wear tests were carried out on fabricated samples, commercial 90WC-Co composites and SS316 materials under the same testing conditions. The volume loss ($V_L$) of the samples after sliding distance of 3000 meters was calculated using Equation 3.2.

$$V_L = {}^{\Delta M}/_{\rho} \tag{3.2}$$

Where ΔM is the change in mass (difference between the initial and the final mass after test) and ρ is the density of the composite [109], [110] .

The specific wear rate of the worn samples was calculated using Equation 3.3 [108, 109].

$$Wear\ rate\ (\frac{mm^3}{Nm}) = \frac{Volume\ loss}{Normal\ load \times Sliding\ distance} \tag{3.3}$$

The wear mechanisms were investigated by examining the morphology of the worn surfaces of the samples after 3000 meters by scanning electron microscopy (CARL ZEISS). Secondary electron (SE) back scattered electron (BSE) and energy dispersive x-ray (EDX) analyses were used.

# 4 RESULTS

## 4.1 Powder microstructure evolution during mechanical alloying

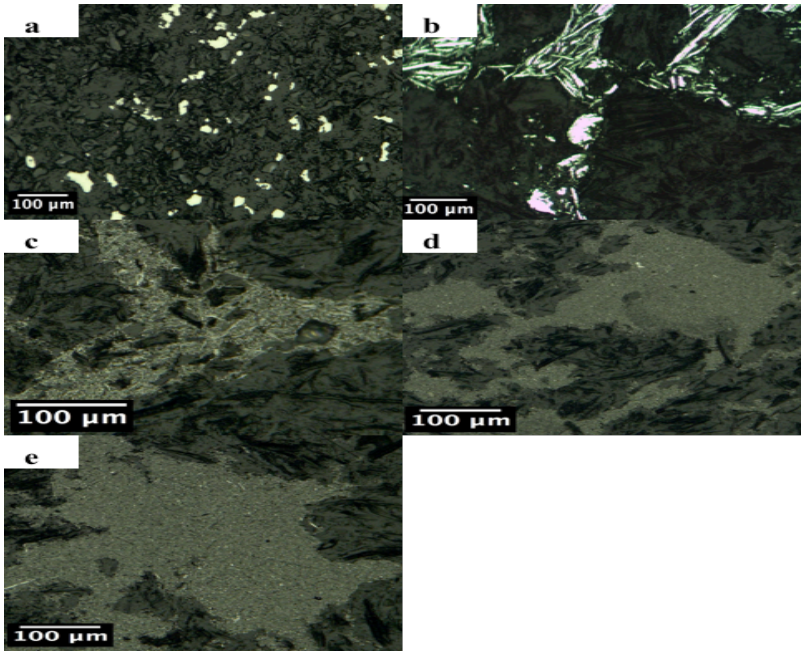


**Figure 4.1: Microstructure evolution during mechanical alloying of SS316L-$Al_2O_3$ powders: (a) As-received; (b) After 10 hrs milling at 720 rpm (SET1A-H); (c) After 20 hrs milling at 720rpm; (d) After 30 hrs milling at 720 rpm; (e) After 20 hrs milling at 800 rpm (SET2A).**

Figure 4.1 shows the optical micrographs of the microstructure evolution of SS316L-$Al_2O_3$ powders during mechanical alloying as a function of milling time and milling speed. For the as-received powder shown in Figure 4.1a, the pure SS316L particles appear brighter with an irregular morphology and aluminum oxide particles are gray and exhibit an angular morphology. After 10 hrs of milling at 720 rpm (SET1A-H) (Figure 4.1b), the microstructure exhibits a lamellar structure as a result of plastic deformation and cold

welding of the SS316L particles [113]. With an increase in milling time to 20 hrs, the lamellar structure is observed to be continuously refined as shown in Figure 4.1c. A homogeneous dispersion of alumina in stainless steel matrix was achieved after 30 hrs of milling at a speed of 720 rpm (SET1A-H, Figure 4.1d) and 20 hrs at 800 rpm (SET2A, Figure 4.1e) for a 1:1 powder–to-powder weight ratio (PPR) and a ball-to-powder ratio (BPR) of 10:1. A uniform distribution of reinforcements is known to result in composites with improved mechanical properties [64], [114]. Please note that the deep dark phase in the images of Figure 4.1 are the epoxy used to mount the samples for metallographic preparation and investigations.

## 4.2 Powder compaction behaviour

Figure 4.2 shows the variation of the powder compaction force with punch displacement for all fabricated SS316L-$Al_2O_3$ composites. The displacement was measured using a linear variable differential transformer (LVDT) and the force was measured using a load cell. For all composite powders the initial stage (0 to 10 mm displacement) occurs at near zero force, as the powder particles rearrange and slide by each other with practically no resistance. The compaction force then increases exponentially in the second stage as the powder agglomerates break and necks are formed between adjacent particles [115]. This is known as the apparent yield point (AYP) that leads to a substantial further increase in green density. Hereby, the broken agglomerates slide into the remaining voids eliminating the inter-agglomerate pores [32], [115]. Finally, the compaction force continues to increase as pores are further closed, powder particles deform and cold hardening takes place. A maximum displacement of 20 mm was reached for SET1 powder. For the SET2C composite powders, the total displacement was 11 mm shorter compared to the SET1 powders. This is

probably due to the longer milling duration and higher milling speed of SET2C leading to a stronger reduction of the particle size and formability of the powder.

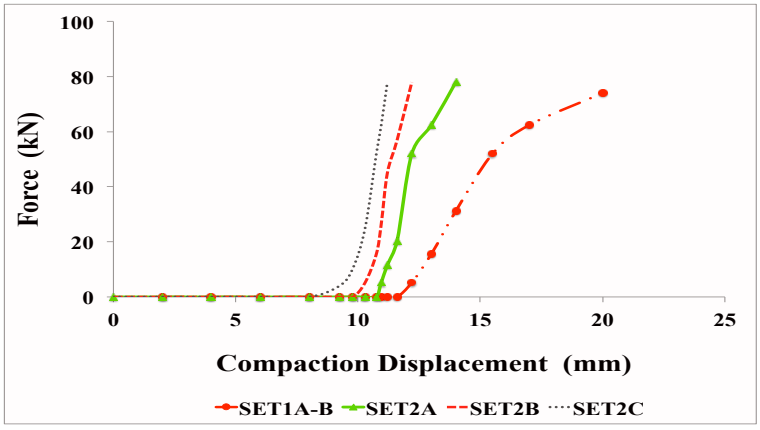


**Figure 4.2: Force-displacement curves during the compaction of SET1A powders (720 rpm for 30 hrs); SET2A (800 rpm for 20 hrs); SET2B (800 rpm for 30 hrs) and SET2C (800 rpm for 50 hrs).**

Figure 4.3 shows the variations of the green densities of the SET1A and SET2A-C samples with compaction pressure. It can be seen that the peak density of 59.0 % is obtained at a compaction pressure of 794.4 MPa for all samples. The increase in green density up to the peak value is due to more advanced closing of gaps between individual powder particles. Beyond the peak value, further increase in compaction pressure leads to sample cracking, primarily during sample ejection, that results in a drop in density.

In addition, air-dried powder seems to yield higher green density compared to the heat dried powder, probably due to the lubrication effect of the remaining milling aid (ethanol) in the powder which reduces friction and improves compressibility during pressing [32]. For the sake of completeness and simplicity, the green densities of SET2B and SET2C were also measured for a 794.4 MPa compaction pressure which is assumed to also apply as

the optimum compaction pressure for these two sets of samples. The results are plotted in Figure 4.3 as well.

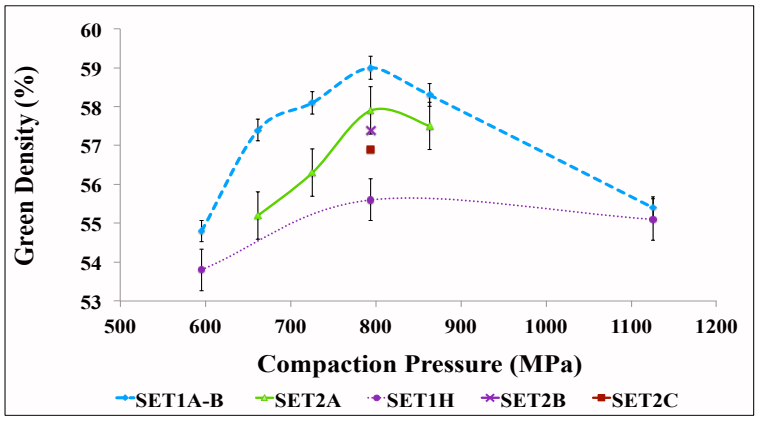


**Figure 4.3: Effects of ball milling parameters, compaction pressure and drying methods on the density of SS316L-$Al_2O_3$ green compacts.**

## 4.3 Sinter behaviour of SS316L-$Al_2O_3$ composites

Samples compacted at the optimum pressure of 794.4 MPa also yielded the highest air sintering density of 66.2 % (SET1H) as shown in Figure 4.4. In contrast to greens, the sinter density of the heat-dried samples was slightly higher compared to air-dried samples. This may be due to the evaporation of remaining milling aid (ethanol) in air-dried samples that results in internal gas pressure and thus hindering densification during sintering.

Overall, solid state sintering in air resulted in lower density due to the presence of oxygen and the relatively lower sinter temperature of 1150 °C compared to the liquid phase sintering in argon at 1400 °C. In liquid phase sintering, the solid grains are surrounded by liquid. The ensuing higher diffusion rates and capillary forces can assist in pulling the grains together by easier sliding and motion of entire grains [116]. In addition, the softening of the

solid grains at high sinter temperatures further promotes grain accommodation and better closing of cavities resulting in enhanced densification [116]. As can be seen in Figure 4.4, the liquid phase sintered samples in argon did show higher sinter density that increased up to the optimum compaction pressure of 794.4 MPa where the highest sinter density of 94.7 % is achieved. The highest density was attained with the SET1B samples. Samples compacted at pressures higher than 794.4 MPa showed excessive plastic deformation, cracking and resulted in lower densities. The difference in the sinter densities between both drying methods was marginal and was in the $\pm$ 0.5 % range. Therefore, the simpler and cost effective air-drying method was chosen for further investigation in this research.

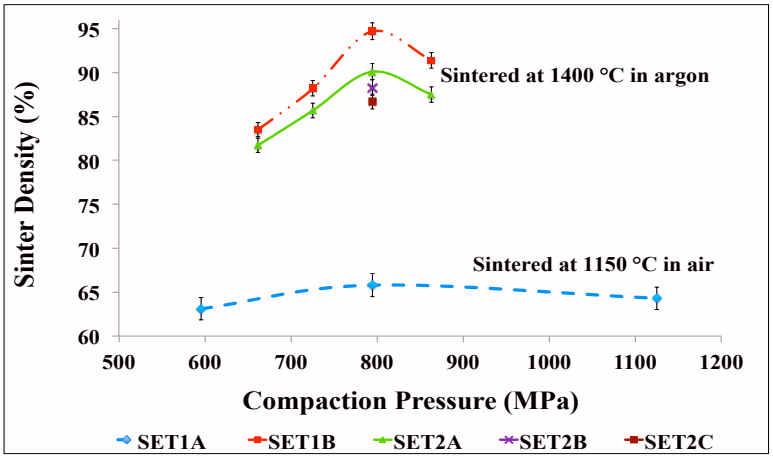


**Figure 4.4: Effects of compaction pressure, powder-drying methods, milling parameters and sinter conditions on the sinter density of SS316L-$Al_2O_3$ composites.**

## 4.4 Microstructural evaluation

### 4.4.1 Optical microscopy analysis

Figure 4.5a shows the micrograph of the homogeneously milled powder for the 720 rpm composite powder. Figure 4.5b shows the green compact at 794.4 MPa containing porosity shown as dark spots. Figure 4.5c shows the air sintered composite with inhomogeneity probably due to the presence of oxygen during sintering causing oxidation with the appearance of bright patches on the surface. The microstructure of the composites sintered in argon atmosphere produced the best microstructure with a homogenous distribution of $Al_2O_3$ particles in the steel matrix as shown in Figure 4.5d.

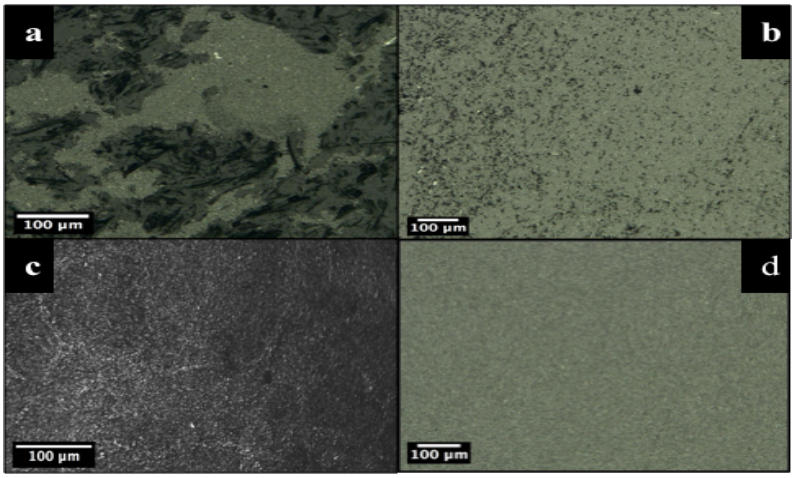


**Figure 4.5: Optical micrograph of SS316L-$Al_2O_3$ composite: (a) Powder after 30 hrs milling at 720 rpm (SET1A); (b) Green compact at 794.4 MPa; (c) Air sintered composite; (d) Argon sintered composite.**

Figure 4.6a shows the microstructure of SS316L fabricated under identical conditions as for the composites. The black spots indicate the presence of pores and inhomogeneity. A refined

improved microstructure was attained as seen in Figure 4.6b with the addition of $Al_2O_3$ particles after sintering.

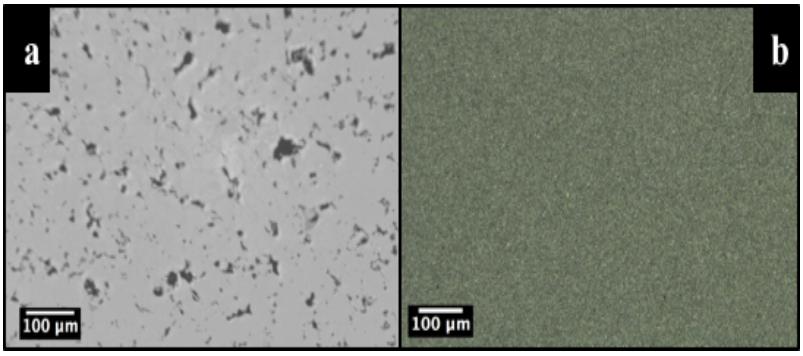


**Figure 4.6: Optical microscopy images of materials fabricated under identical compaction (794.4 MPa) and sinter conditions (1400 °C in argon): (a) SS316L; (b) Fabricated SS316L-$Al_2O_3$ composites.**

### 4.4.2 Homogeneity of the microstructure

Figure 4.7a shows the chemical composition of the sintered composites as determined using SEM EDX (Energy-dispersive x-ray spectroscopy). The brighter phase is SS316L and contains iron, chromium and Nickel with elemental weight percentage as tabulated in Table 4.1. The relatively high O and Al contents shown in Table 4.1 reflect the fact that the EDX spots during analysis did cover some $Al_2O_3$ particles embedded in the matrix. The chemical composition of the alumina particles in the SS316L-$Al_2O_3$ composites is shown in Table 4.2. Here again, the relatively high contents of Fe, Cr and elements other than Al and O reflect the size of the EXD analysis spots that cover the steel matrix surrounding the $Al_2O_3$ particles.

**Table 4.1: Chemical composition of the SS316L matrix with some few embedded $Al_2O_3$ particles.**

| Elements | O | Al | Cr | Ni | Fe |
|---|---|---|---|---|---|
| Wt. % | 3.51-5.01 | 3.94-6.05 | 14.86-16.90 | 10.65-12.5 | Balance |

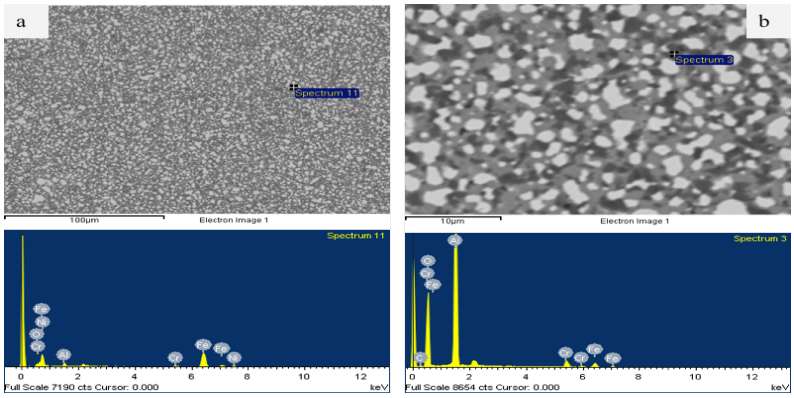


**Figure 4.7: SEM EDX area mapping and point spectrum analysis on sintered SET1B composites: (a) brighter steel matrix phase; (b) darker alumina particles.**

**Table 4.2: Chemical composition of alumina particles in SET1B with some surrounding steel matrix.**

| Elements | Al | O | Fe | Cr | Others |
|---|---|---|---|---|---|
| Wt. % | 36.56-40.62 | 36.98-41.09 | 6.5-8.12 | 6.34-7.93 | 1.79-2.24 |

**Table 4.3: Chemical composition of MA SET2C composites.**

| Elements | O | Al | Fe | Cr | Others |
|---|---|---|---|---|---|
| Wt. % | 18.67-22.74 | 21.88-26.75 | 27.62-30.62 | 13.09-16.66 | 2.1-3.8 |

Figure 4.8 shows the EDX area analysis of the SET2C (800 rpm for 50 hrs) powder after mechanical alloying. The elemental compositional is given in Table 4.3.

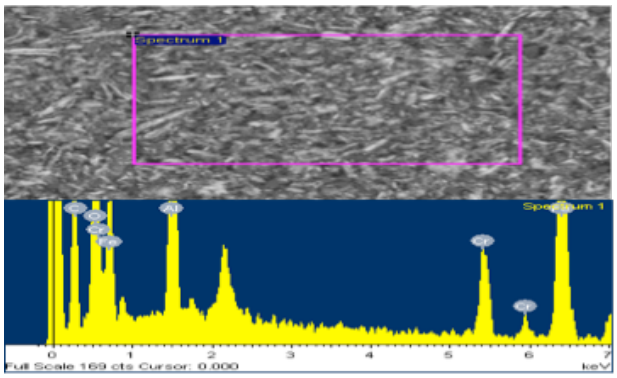


**Figure 4.8: SEM EDX area mapping of MA SET2C powder composites.**

### 4.4.3 Porosity analysis

The porosity analysis was done on SEM micrographs using the Image J software. The theoretical porosity was calculated as 5.3 vol.% and the porosity percentage from the Image J software was approximately 5.5 vol.% for the fabricated SET1B.

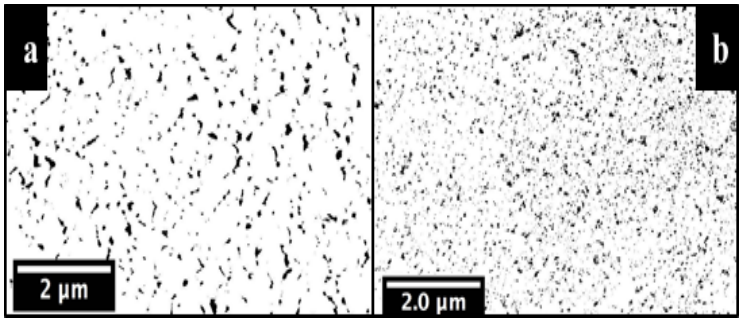


**Figure 4.9: Porosity contrast on samples using SEM microscopy and the Image J software: (a) SET1B; (b) SET2C.**

The image J software images showing the porosity in SET1B and SET2C composites are shown in Figures 4.9(a-b), respectively. As expected, all sintered samples showed lower porosity as compared to the green compacts, which illustrates the success of the sintering process both in air and under argon atmosphere.

As can be seen in Figures 4.10 and 4.11, the samples compacted at the optimum pressure of 794.4 MPa showed the lowest porosity.

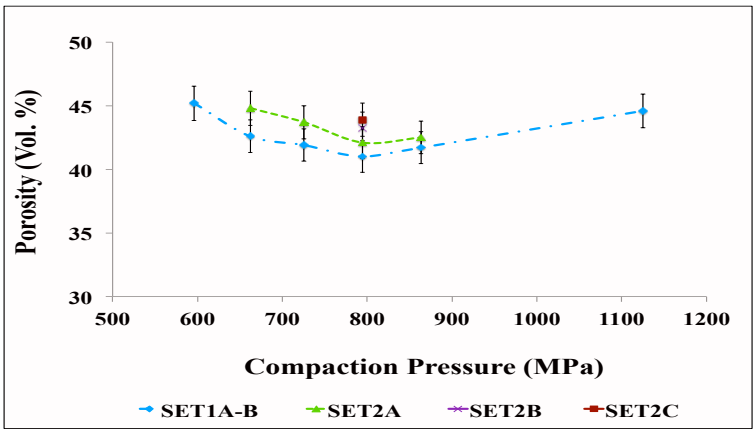


**Figure 4.10: Porosity of SS316L-$Al_2O_3$ green compacts as a function of compaction pressure and milling parameters.**

Compared to all other composites, SET1B (720 rpm for 30 hrs) samples showed the lowest porosity in both the green and sintered state.

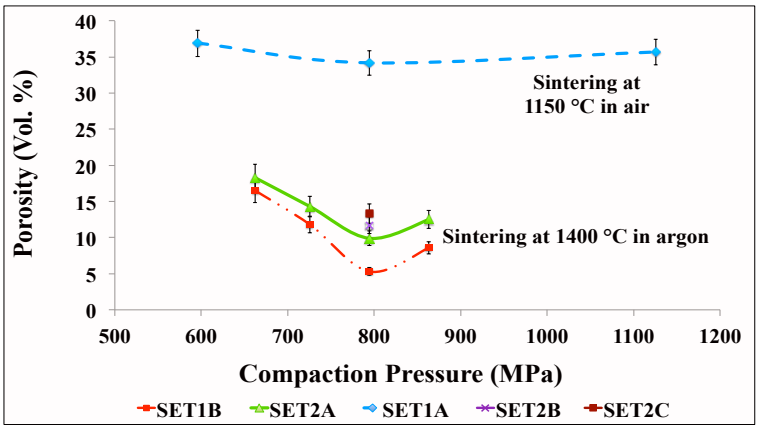


**Figure 4.11: Porosity of sintered SS316L-$Al_2O_3$ composites as a function of compaction pressure, milling parameters and sinter conditions.**

## 4.5 Mechanical properties

### 4.5.1 Hardness

Figure 4.12 shows the green hardness as a function of milling parameters and compaction pressure. It is observed that as the compaction pressure increases, the hardness first increases and then decreases with the peak hardness achieved at the optimum compaction pressure of 794.4 MPa. The SET2A-C samples showed that excessively long milling durations could lead to decreased hardness as seen on SET2B and C (800 rpm for 30hrs and 50 hrs) greens measured at the optimum compaction pressure. This is primarily due to contamination from the steel milling balls. SET2C (800 rpm for 50 hrs) samples had the lowest green hardness.

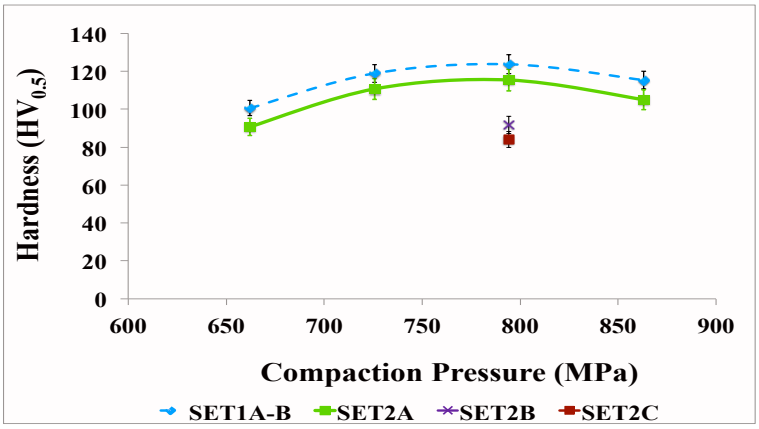


**Figure 4.12: Variation of the green hardness as a function of compaction pressure and milling parameters.**

The results of the hardness after sintering are shown in Figure 4.13. It is observed that the highest hardness was attained at the optimum compaction pressure of 794.4 MPa for all two sinter conditions. Sintering at 1400 °C in argon atmosphere and milling at the 720 rpm for 30 hrs (SET1B) provided the overall highest hardness.

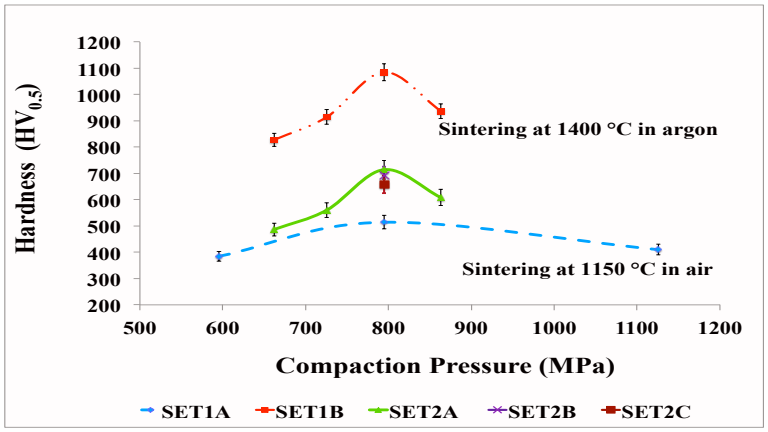


**Figure 4.13: Variation of sinter hardness of SS316-$Al_2O_3$ composites as a function of compaction pressure, milling parameters and sinter conditions.**

The sinter hardness decreases for compaction pressures beyond 794.4 MPa similar to the trend for the green hardness. The superior hardness exhibited by the SET1B composites is due to the absence of oxygen, better evaporation of milling aid (ethanol), controlled argon atmosphere and higher temperature of 1400 °C during sintering as well as less contamination during milling.

### 4.5.2 Fracture toughness

The fracture toughness of the composites was obtained from Vickers indentation testing under a 5 kgf load. The crack length and the indentation diagonal were used. At low loads the Palmqvist crack mode prevails [117] as the c/a ratio was determined to be approximately 1.7, which is below the transition value of 2.5 [108], [118].

**Table 4.4: A comparison of different modeling approaches for estimating the composite fracture toughness.**

| Eqn. No | Crack Types | Ref. | $K_{IC}$ Equations | SET1B (720 rpm, 30 hrs, 794.6 MPa, 1400°C, Argon). MPa√m | SET2A (800 rpm, 20 hrs, 794.6 MPa, 1400°C, Argon). MPa√m | b |
|---|---|---|---|---|---|---|
| 1 | Palmqvist | [106] | $K_{IC} = 0.0515\frac{F}{c^{3/2}}$ | 3.7 | 2.4 | 37 |
| 2 | Palmqvist | [106] [107] | $K_{IC} = 0.079\frac{F}{a^{3/2}}\log(4.5\frac{a}{c})$ | 30 | 23.7 | 5.2 |
| 3 | Palmqvist | [117] | $K_{IC} = 0.0246\left(\frac{E}{HV}\right)^{2/5}(HV.F)^{1/2}$ | 1.8 | 1.7 | 45 |
| 4 | Palmqvist | [117] | $K_{IC} = 0.0889(HV.F)^{1/2}$ | 2 | 1.7 | 44 |
| 5 | Median | [106] | $K_{IC} = 0.0726\frac{F}{c^{3/2}}$ | 5.2 | 3.3 | 32 |
| 6 | Median | [117] [68] | $K_{IC} = 0.016\left(\frac{E}{HV}\right)^{1/2}\frac{F}{c^{3/2}}$ | 5.0 | 3.9 | 31 |
| 7 | Median | [117] [68] | $K_{IC} = 0.028\,(HV.a^{1/2})\left(\frac{E}{HV}\right)^{1/2}\left(\frac{c}{a}\right)^{-3/2}$ | 3.9 | 3.2 | 35 |
| 8 | Median | [117] | $K_{IC} = 0.010\left(\frac{E}{HV}\right)^{2/3}\frac{F}{c^{3/2}}$ | 11.6 | 10.8 | 18 |
| 9 | Median | [106] | $K_{IC} = 0.014\left(\frac{E}{HV}\right)^{1/2}\frac{F}{c^{3/2}}$ | 5.4 | 3.5 | 31 |
| 10 | Curve-fitting | [106] | $K_{IC} = 0.0089\left(\frac{E}{HV}\right)^{2/5}\left(\frac{F}{a.c^{1/2}}\right)$ | 3.6 | 2.9 | 35 |
| 11 | Curve-fitting | [106] | $K_{IC} = 0.018\left(\frac{E}{HV}\right)^{1/2}\frac{P}{c^{3/2}}$ | 12.7 | 11 | 17 |
| 12 | Curve-fitting | [106] | $K_{IC} = 0.0889\left(\frac{HV.F}{\sum_{i=1}^{4} c_i}\right)^{1/2}$ | 8.8 | 8.0 | 22 |

Experimental data yielded fracture toughness values of 30 MPa√m and 23.7 MPa√m for SET1B (720 rpm for 30 hrs) and SET2A (800 rpm for 20 hrs) composites respectively as seen in Table 4.4.

Table 4.4 summarizes the model approaches used to estimate the fracture toughness. The parameters used include the indentation test load F; the Vickers hardness HV; the indentation half-length diagonal a; the elastic modulus E; and the crack length c. The variations in the calculated fracture toughness values in the Table 4.4 results from the different types of crack formation modes and models used. Equation 2 applies to the Palmqvist crack mode observed on the investigated composites. As such, it proved to better

represent the fracture toughness of the composites after validation using Equations 5.2 and 5.4 as discussed in section 5.4.

Figure 4.14 shows an optical microscopy of the Vickers indentation on a SET1B composite. At least ten (10) indents were measured to calculate the average fracture toughness value according to the Evans and Wilshaw model as seen in Equation 3.1 [107].

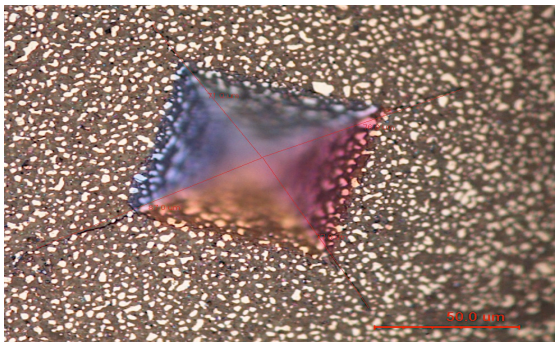

**Figure 4.14: Crack length measurement on a SET1B (720 rpm 30 hrs) composite for the Vickers indentation fracture toughness test.**

### 4.5.3 Wear resistance

Figure 4.15 shows the volume loss versus the compaction pressure for SET1B and SET2A-C samples. It can be observed that the volume loss for SET1B samples decreases as the compaction pressure increases up to the optimum compaction pressure and then increases slightly with further increase in compaction pressure. The lowest volume loss of 11.9 $mm^3$ was measured on SET1B and was 2.8 times lower than that of the best composites from powders milled at 800 rpm (SET2A). As can be seen in Figure 4.16, this also translates into a 5 and 7.3 times decrease in volume loss compared to the commercial SS316 and unreinforced SS316L fabricated under identical conditions.

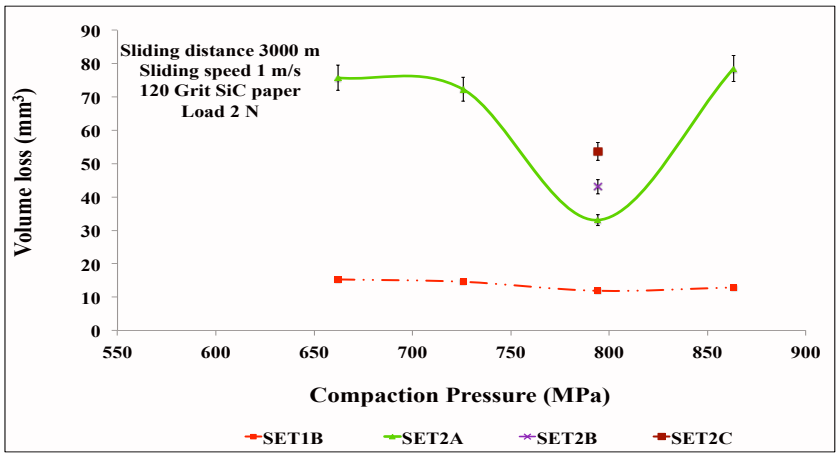


**Figure 4.15: Effects of compaction pressure, milling parameters and sinter conditions on the dry abrasive volume loss of SS316L-$Al_2O_3$ composites.**

However, compared to commercial 90WC-Co, 6 times and 16.6 times higher volume loss was measured for SET1B (720 rpm for 30 hrs) and SET2A (800 rpm for 20 hrs) at a sliding distance of 3000 meters.

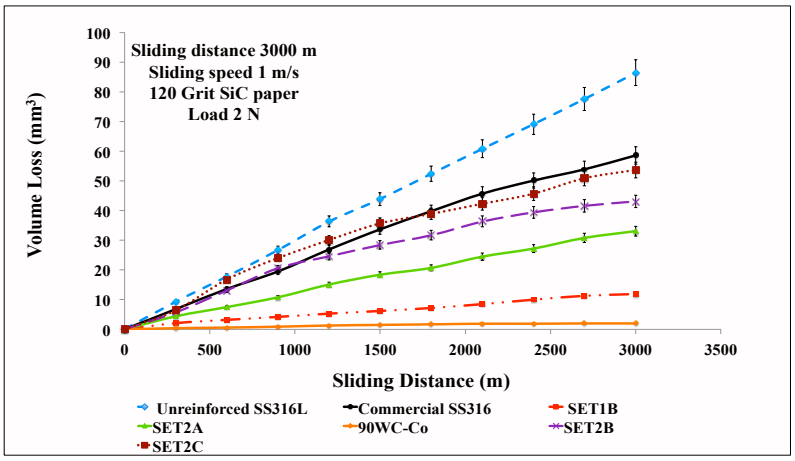


**Figure 4.16: Comparative plot of volume loss against sliding distance for fabricated unreinforced SS316L, SS316L-$Al_2O_3$ composites (SET1B, and SET2A-C), commercial SS316 and 90WC-Co composite.**

This corresponds to an increase in wear rate by 83.2 % for SET1B and 94 % for SET2A.

SET1B had a wear rate of 0.004 $mm^3/m$ compared to the least worn SET2A (800 rpm for 20 hrs) sample with a wear rate of 0.011 $mm^3/m$, commercial SS316 with a wear rate of 0.0195 $mm^3/m$ and the fabricated unreinforced SS316L with a wear rate of 0.0288 $mm^3/m$.

### 4.5.4 Wear patterns

Figure 4.17 shows SEM micrographs of worn surfaces of the SET1B (720 rpm for 30 hrs) and SET2A-C (800 rpm samples) composites. Wear takes place primarily by micro cutting with occasional chips, ploughing and grain pull out as seen along the sharp grooves or wear track primarily observed on the SET2B-C (800 rpm for 30 hrs and 50 hrs) worn surfaces (Figures 4.17c-e).

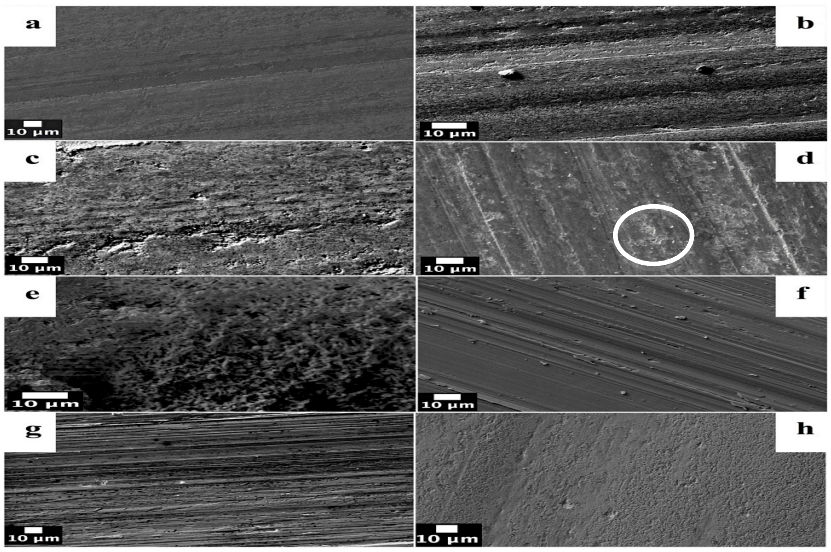


**Figure 4.17: SEM image of the composite worn surfaces: (a) SET1B; (b) SET2A; (c) SET2B; (d) SET2C; (e) A magnified image of wear scar in figure 4.17d; (f) Unreinforced SS316L; (g) Commercial SS316; and (h) Commercial 90WC-Co.**

From the SEM images of the fabricated SS316L and the commercial SS316 samples (Figures 4.17f and 4.17g), it is seen that both are typified by extensive plastic deformation

and relatively rapid material removal characterized by deep grooves, smearing, and indentation pits. Figure 4.17h shows the wear patterns for the commercial 90WC-Co composite. The worn surface exhibits only few wear scratches and grooves characteristics for slow material removal.

### 4.5.5 Wear surface profile

Figures 4.18-4.24 below show the wear profile of the worn surface after each wear testing for the various fabricated composites, commercial samples and unreinforced SS316L. SET1B (Figure 4.18) showed the lowest wear scar depth compared to the other fabricated materials, and 90WC-Co samples had the overall lowest wear scar depth.

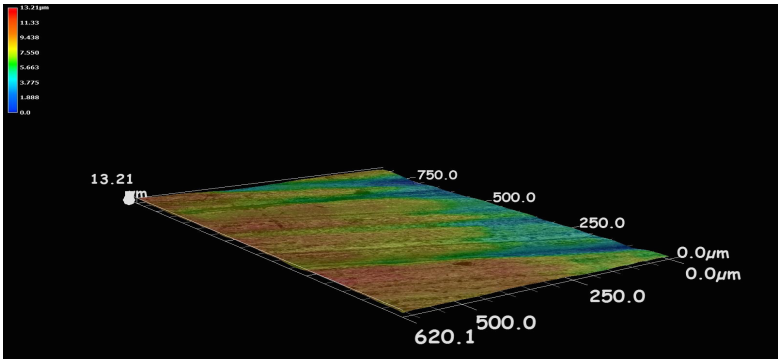


**Figure 4.18: Wear surface profile of SET1B (720 rpm for 30 hrs) composite.**

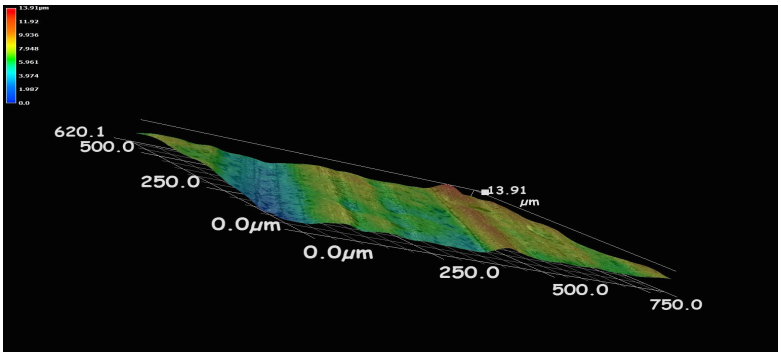


**Figure 4.19: Wear surface profile of SET2A (800 rpm 20 hrs) composite.**

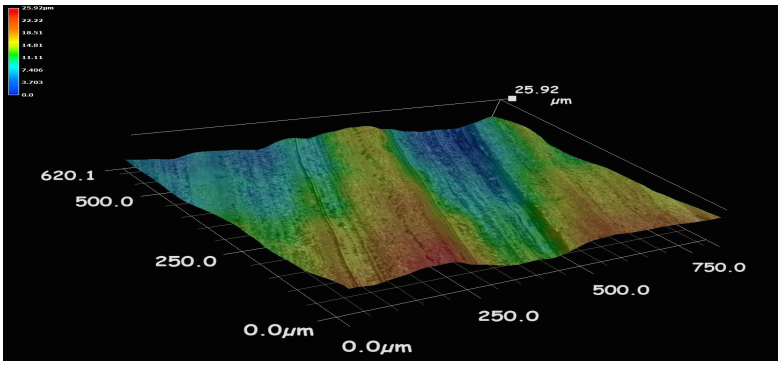


**Figure 4.20: Wear surface profile of SET2B (800 rpm for 30 hrs) composite.**

This higher wear resistance of WC-Co composites is probably due to the lower Ha/Hc ratio compared to the other materials, as well as to its higher ceramic content (90 wt.%) compared to the fabricated composites (50 wt.%). Figure 4.22 shows the surface profile of the fabricated unreinforced SS316L after the wear testing. Macro-surface scars were observed with the highest wear depth as a result of its low hardness compared to the hardness of the SiC abrasive disk.

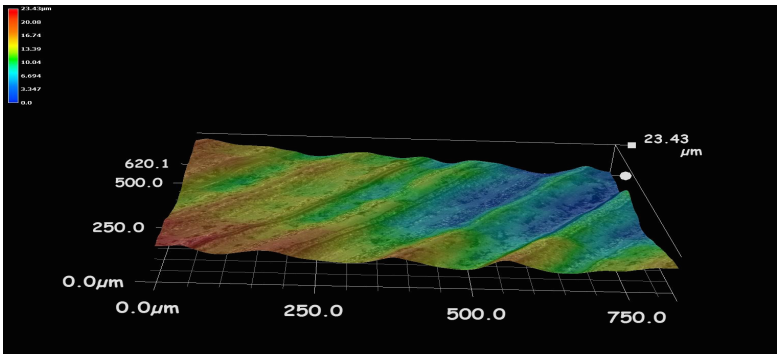


**Figure 4.21: Wear surface profile for SET2C (800 rpm for 50 hrs) composite.**

As a result, the rate of material removal was higher (approximately 0.0288 $mm^3/m$) compared to the fabricated composites. The wear groove depth for the SS316L was 11 µm compared to the groove depth for the best fabricated composite SET1B (720 rpm for 30 hrs)

with a groove depth of 2.3 µm as seen in Figure 4.18. This corresponds to groove depth reduction by 79.1 %.

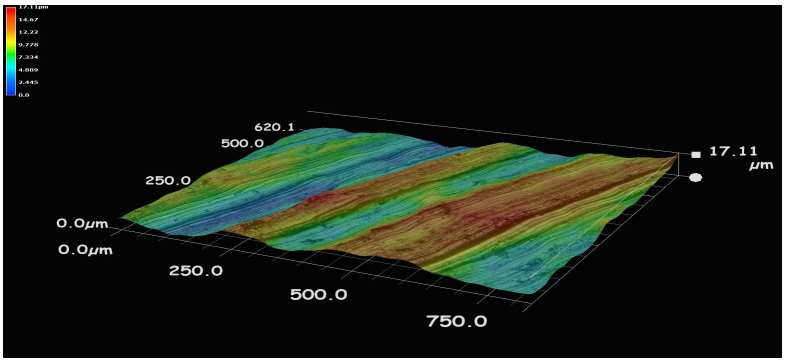


**Figure 4.22: Wear surface profile of unreinforced SS316L.**

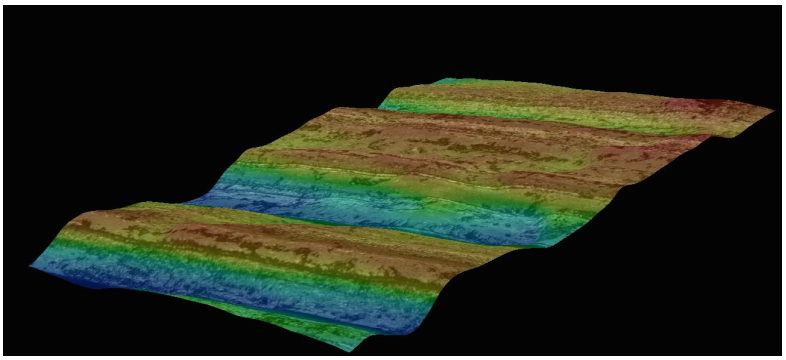

**Figure 4.23: Wear surface profile of commercial SS316.**

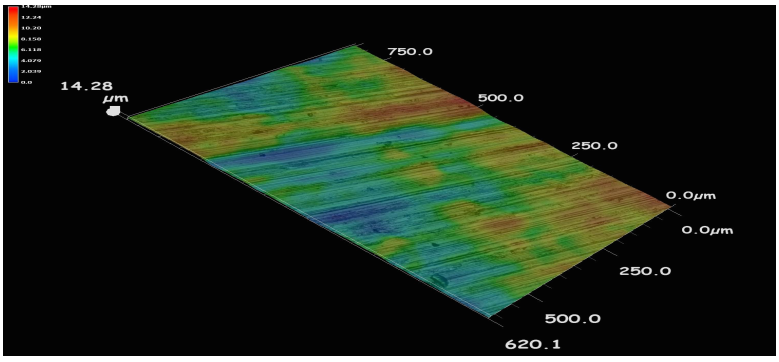


**Figure 4.24: Wear surface profile of commercial 90WC-Co composite.**

# 5 DISCUSSION

## 5.1 Effects of $Al_2O_3$ particle addition in SS316L

The overall effect of $Al_2O_3$ particles on the wear resistance of SS316L depends on the achieved changes in both hardness and toughness [119]. In this study, the addition of $Al_2O_3$ to SS316L led to a drastic increase in hardness from 121 HV to 1085 HV. This increase by a factor of 9 can be expected to substantially limit indentation, plug-in and ultimately wear loss [28], [102], [114]. The effect of $Al_2O_3$ addition on the fracture toughness of SS316L is more nuanced and depends strongly on the processing parameters, primarily on the uniformity of the reinforcement particle distribution. While SS316L-$Al_2O_3$ composites generally show a decrease in toughness compared to unreinforced SS316L, a refined and more homogeneous microstructure as seen in Figure 5.1 can provide an optimum combination of hardness and toughness resulting in excellent wear resistance [21], [28], [43], [102], [120]. The brighter phase is steel and the darker phase is alumina as seen in Figure 5.1.

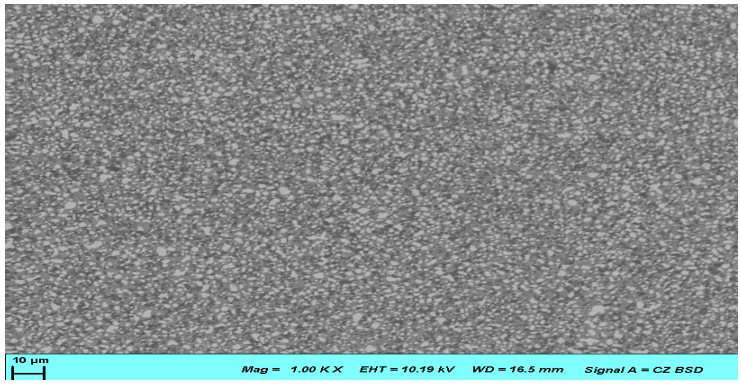


**Figure 5.1: Homogeneous microstructure of SET1B composites.**

On the other hand, $Al_2O_3$ particles addition reduces compressibility leading to increased porosity and lower density. This is most likely due to the inherently higher hardness of $Al_2O_3$ and its action as dislocation barriers that reduce the deformability and ductility of the composite powders [21], [102]. Furthermore, alumina particles tend to locate at grain boundaries, which tends to produce a weak interfacial strength resulting in easy crack initiation and lower toughness [121]. This result in easier surface material removal during wear loading by cracking or fragmentation of the heavily deformed subsurface [83], [122]. Therefore, the overall improvement of the tribological properties of the composite depends on the amount, size, shape and distribution of the dispersed second phase particles [123]. In this respect, previous literature reported that the addition of 5 wt.% $Al_2O_3$ improved the wear resistance of 304L stainless steel by factor 3.5 and that of SS316L by factor 2 [67]. For the present work, an improvement by factor 7.3 was achieved with the addition of 50 wt.% $Al_2O_3$.

**Table 5.1: Wear coefficients (K) of different steels and cermets.**

| No. | Ref. | Materials | K | Types of abrasive | Types of test |
|---|---|---|---|---|---|
| 1 | [78] | Mild steel | $7 \times 10^{-3}$ | Tool steel | Pin-on-disk |
| 2 | [78] | Hard tool steel | $1.3 \times 10^{-4}$ | Tool steel | Pin-on-disk |
| 3 | [78] | Ferritic stainless steel | $1.5 \times 10^{-5}$ | Tool steel | Pin-on-disk |
| 4 | [78] | Sintered WC-Co | $4 \times 10^{-6}$ | Mild steel | Ring-on-ring |
| 5 | [62] | SS304-$TiB_{2\text{-HIP}}$ | Range $10^{-5}$ | SiC | Pin-on-disk |
| 6 | [60] | WC-Co | Range $10^{-7}$ | Silica sand | Block-on-ring |
| 7 | Research Materials | SS316L | $1.4 \times 10^{-2}$ | SiC | Pin-on-disk |
| 8 | | SS316L-$Al_2O_3$ | $1.9 \times 10^{-3}$ | SiC | Pin-on-disk |
| 9 | | Commercial WC-Co | $3 \times 10^{-4}$ | SiC | Pin-on-disk |

For comparison, the wear coefficients (K) of different steels and cermets are summarized in Table 5.1. It shall be noted that the wear coefficient can be affected by both the material composition as seen for the different steels and the wear test conditions such as the type of abrasive and the test set-up.

## 5.2 Effects of fabrication parameters

The optimum compaction pressure was found to be 794.4 MPa, which yielded a sinter density of 94.7 % and the highest sinter hardness of 1085 HV (for SET1B powder: 720 rpm for 30 hrs). This compaction pressure represents the optimum balance between improved densification with increasing pressure and the limitation of defects such as cracks created at excessively high pressures. Moreover, the lower milling speed of 720 rpm results in relatively larger composite powder particles that favor plastic deformation and densification during compaction [32], [115], [124].

As the milling speed increases, the composite powders and the alumina particles tend to undergo more cold work and excessive refinement [125] resulting in harder powders with reduced compressibility, ultimately leading to lower sinter density. Overall, ball milling initially refines, embeds and distributes the $Al_2O_3$ particles in the steel matrix yielding composites with improved properties. However, longer milling durations lead to more contamination and deteriorated hardness and wear resistance [14], [126], [127].

The samples sintered at 1400 °C showed the highest sinter density, hardness and wear resistance as the sintering temperature has a strong effect on the diffusivity and neck growth [104], [128]. Specifically for the fabricated SS316L-$Al_2O_3$ composites, 1400 °C is slightly above the melting point of the steel matrix, which led to liquid phase sintering and the observed lowest porosity and highest densification. Similarly, the samples sintered in

argon had better microstructure, mechanical properties and higher density as a result of reduced oxidation. As the sinter chamber was first evacuated prior to introducing argon, improved degassing by evaporation of the milling aid (ethanol) also contributed to the better properties of argon sintered composites.

Figure 4.15 shows the abrasive volume loss as a function of compaction pressure. It can be seen that the wear rate decreases with increasing compaction pressure. However, beyond the optimum compaction pressure, the wear rate increases as a result of pre-damage and pre-cracks causing higher porosity and lower hardness in the samples (Figures 4.11 and 4.13). It is also observed that with an increase in hardness, the wear rate decreases (Figure 5.2) according to the tribology principle that wear is inversely proportional to hardness (Equation 2.1) [129], [130].

### 5.3 Correlation between hardness and wear resistance

The best composite (SET1B) shows a significant increase in micro hardness by approximately factor 9 compared to unreinforced SS316L primarily due to the addition of $Al_2O_3$ particles. This resulted in a reduction in wear volume loss by 86 % when compared to the unreinforced matrix. The much higher wear rates of unreinforced steel (commercial and lab fabricated) are due to their much lower hardness (121 HV) compared to the SiC abrasive used for wear testing with a hardness of 2500 HV. The abradents can therefore remove material more rapidly from the wear surface [6] by deep plug-in and rapid micro-cutting [67]. The lower composite hardness resulting from higher milling speed and excessive milling duration also led to lower wear resistance as seen in Figure 5.2 showing the comparative plot between the specific wear rates and the hardness of the various fabricated and commercial composites. Here, lower hardness and wear resistance are primarily due to

contamination and excessive refinement of $Al_2O_3$ particles. The potential increase in wear rate caused by ultrafine particles when tested using coarsed abrasives was earlier reported in literature [69], [80], [131], [132]. It was rationalized by the fact that fine particles easily detach from the matrix during wear due to the smaller interface area between the binder phase and the hard particle. Also, finer $Al_2O_3$ particles tend to dissolve faster during sintering leading to a stronger formation of brittle oxide and alumide phases and ultimately to reduced toughness and wear resistance.

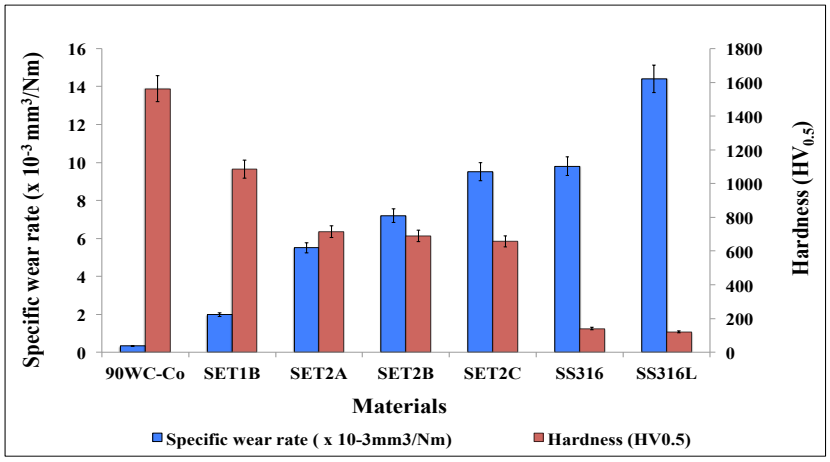


**Figure 5.2: Comparative plot of specific wear rate and hardness of fabricated unreinforced SS316L, commercial SS316, fabricated SS316L-$Al_2O_3$ composites (SET1B, and SET2A-C) and commercial 90WC-Co composite.**

The relationship between the hardness and the wear rate is nonlinear. At the same level of hardness, the wear resistance may differ by up to 50 % [123], [129], [133]. This is because the wear resistance depends on both the hardness and the toughness [69], and an increase in hardness mostly leads to some reduction in toughness. Therefore, an optimum balance must be obtained to prevent the material from being either too soft or too brittle.

## 5.4. Effect of porosity on fracture toughness, Young's modulus and wear rate

Using the rule of mixture and toughness values of SS316L and $Al_2O_3$ obtained from literature [134], [135], the theoretical composite toughness was estimated to be 39.64 MPa√m. However, experimental toughness values of 30.0 MPa√m and 23.7 MPa√m were determined for SET1B and SET2A using the indentation method, respectively, as seen in Table 4.4. The rule of mixture is accurate for dense and non-porous materials when the relative density is close to 100 % [119]. However, the SET1B samples had 5.3 vol.% porosity, which seems to result in the observed 24 % toughness drop. Similarly, SET2A samples had a porosity of 9.9 vol.% leading to the observed 40 % drop in toughness. This can be rationalized by the action of flaws and pores as crack initiation sites or stress raisers in the composites [136]. Chmielewski et al. [137] reported a similar effect of porosity in Molybdenum composites containing 25 % and 40 % $Al_2O_3$ with a drop in fracture toughness between 22 and 27 %. The effect of porosity on the fracture toughness was described in earlier literature using Equations 5.1 and 5.2 suggesting an exponential relationship [91], [138]–[141].

$$\boldsymbol{K_{IC(p)} = K_{IC(0)}\,(1 - P)^{m+0.5}} \tag{5.1}$$

$$\boldsymbol{K_{IC(p)} = K_{IC(0)} \exp\,(-bP)} \tag{5.2}$$

Where $K_{IC(p)}$ is the fracture toughness of the porosity containing composite and $K_{IC(0)}$ is the fracture toughness of the dense material without porosity calculated from the rule of mixture; P is the porosity; t = m+0.5; t is the exponent and m is an empirical constant depending on the fabrication parameter, shape and distribution of pores. When low porosity is assumed (≤10 % or 0.1), Equation 5.1 is reduced to Equation 5.2 [141] and the empirical

constant b is the same as the exponent t described above [141], [142]. The estimated b values are provided in Table 4.4. Equation 5.2 was used in this study, as the remaining porosity was less than 10 vol.%.

Similar to the toughness, the Young Modulus can be related to the porosity as in Equation 5.3 [134], [136], [139], [141]–[144].

$$\boldsymbol{E_{(p)} = E_{(0)}(1 - P)^m} \tag{5.3}$$

$$\boldsymbol{E_{(p)} = E_{(0)} \exp(-bP)} \tag{5.4}$$

Where $E_{(p)}$ is the Young's modulus of the experimental material with porosity; $E_{(0)}$ is the Young's modulus of the fully dense material; P is the porosity; and m is an empirical constant. The elastic modulus was calculated using Equations 5.4. The relative elastic modulus from Equations 5.3 and 5.4 and the relative fracture toughness from Equations 5.1 and 5.2 were found to be in agreement with experimental data for m = 4.7 and b = 5.2. This value of the constant b is within the expected range as can be seen in Table 4.4. For most properties such as the compressive strength, the hardness and the wear for which the primary mode of loading is compressive, greater porosity dependence is observed with b values in the range of $6 \pm 3$. Spriggs et al. [139] reported the relationship between the elastic modulus (E) and the porosity (P) for polycrystalline alumina. They observed that the porosity range has a significant influence on the empirical factor b, which also depends on fabrication parameters as well as on the shape and distribution of pores [139], [145].

The porosity has long been linked to the degradation of the strength, hardness and toughness of materials. Yet, little has been done on the influence of the porosity on the wear resistance [133], [146], [147]. As can be seen in Figure 5.3, the results of this study show

that the wear rate increases with increasing porosity as also reported in literature [148]. This will be further discussed in subsection 5.8.

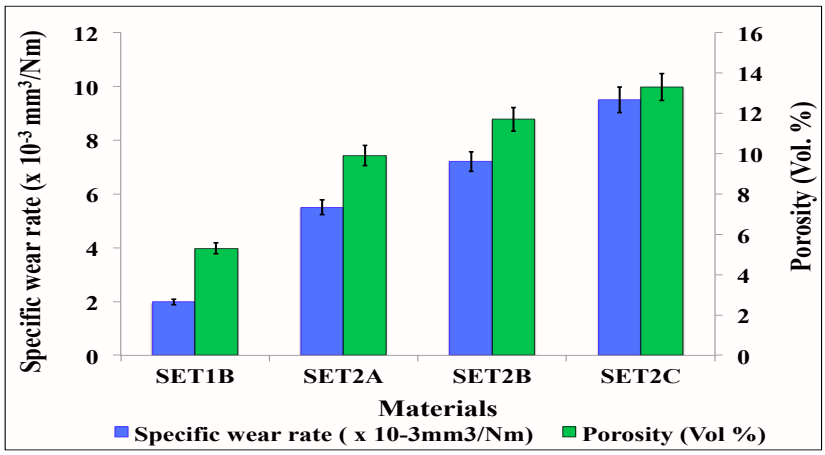


**Figure 5.3: Porosity and wear rate for the fabricated SS316L-$Al_2O_3$ composites.**

## 5.5 Abrasive wear of SS316L-$Al_2O_3$ composites

The SEM images of the wear scar surfaces (Figures 4.17a-h) confirm that the material removal depends on the material type, hardness and fabrication parameters. For the SET2A-C samples with lower hardness (Figures 4.17b-g), micro cutting with deep grooves and pullout of the $Al_2O_3$ particles was the dominant mechanism. Plastic deformation and fatigue due to the repeated indentation by abrasive particles lead to rapid material removal followed by the weakening of the steel matrix-alumina particles interface bonding. This results in the eventual pullout of the reinforcement particles [149], [150] as seen in the worn surface images (Figures 5.4a-b). The SiC abrasive particle indentation into the unreinforced steel materials was largely due to a high degree of plastic deformation resulting from the much lower hardness of the steel. This in turn results in severe wear compared to the fabricated composites. The higher hardness of the composites allowed only micro ploughing

and scratches on the sample surfaces producing shallow groves as seen in the images of the wear scars for the fabricated SET1B and commercial 90WC-Co composites (Figures 4.17a and 4.17h). This is in agreement with literature reports that the wear rate decreases with the reduction in the binder phase volume fraction and the hardness increases with the increase in ceramic phase content [120], [129], [137].

The wear rate decreases as the sliding distance increases. This can be due to strain hardening effects, sample realignment and increase in effective sample surface hardness as the steel matrix is preferentially removed exposing the harder alumina particles. All fabricated composites exhibited similar wear mechanisms as discussed earlier and seen in Figures 4.17(a-d).

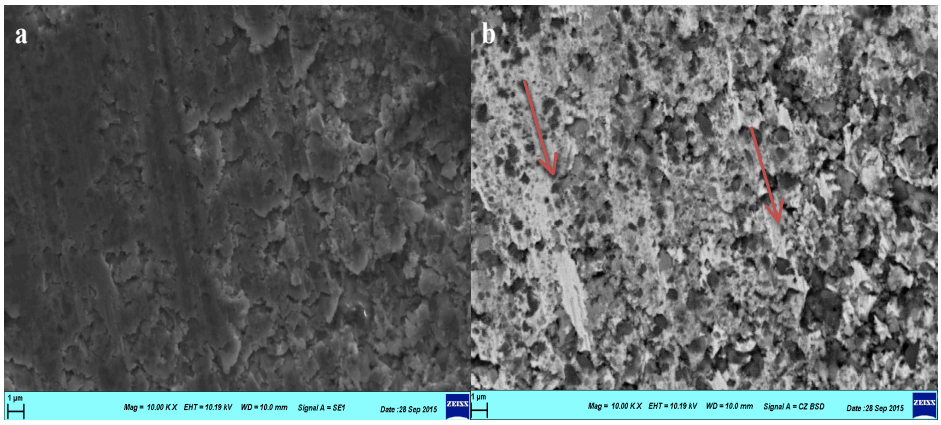


**Figure 5.4: Images of worn surfaces of SET2C: (a) SEM; (b) BSD.**

Though, the difference in scar penetration depth varied from material to material. Among the composites, the highest mass loss was recorded on SET2C (800 rpm for 50 hrs) samples probably as a result of the high milling intensity and long milling duration that led to high contamination, excessive cold work and excessive refinement of the $Al_2O_3$ particles. Ultrafine reinforcement particles provide low wear resistance against coarse abrasives [127],

[149]. The movement of the abrasive particles over the surface of the samples resulted in the distortion of the matrix (SS316L) along the sliding direction (arrows) as seen in Figure 5.4b. In this Figure, the dark spots reveal $Al_2O_3$ particles and the lighter spots show the SS316L matrix.

## 5.6 Abrasive wear models

There have been numerous attempts to predict abrasive wear rates using different methods as discussed in chapter 2. Most of the wear models primarily relate the material loss to the mechanical properties and wear conditions involving either two or more bodies in relative motion. For two or three body abrasive wear, the Archard model (Equation 2.1) together with the Rabinovicz model [4], [77], [78], [151], [152] are the most widely accepted approaches. However, both consider neither the fracture toughness nor microstructure parameters in their approach.

## 5.7 Analysis of the different abrasive wear models

The Archard wear model (Equation 2.1) is predominantly used for sliding wear by micro cutting or/and ploughing by hard abrasives on a soft material [153]. In this study, it was used to calculate the specific wear rates for SET1B (720 rpm for 30 hrs) and SET2A (800 rpm for 20 hrs). The challenge with the Archard wear model is the unknown value of the wear coefficient K that can only be determined experimentally although Bodhak et al. reported that K typically ranges between $10^{-6}$ and $10^{-1}$ [88]. Also, it does not include the fracture toughness [154], [155] or any microstructural parameters. Equations 2.5 and 2.8 represent improved formulations in this aspect. They assume that the wear rate is

proportional to the applied load and inversely proportional to the product of the hardness and fracture toughness.

Equation 2.6 looks at the relationship between the abrasive wear resistance (reciprocal of wear rate) and the abrasion parameter (AP) defined as in Equation 5.5. The abrasive wear resistance is directly proportional to the abrasion parameter. The uniqueness of this equation is the consideration of the grain or strengthening particle size $D_c$ as microstructural parameter, suggesting that smaller grains or strengthening particle sizes can lead to higher abrasion parameter and wear resistance [86].

$$\boldsymbol{AP = \frac{K_{IC}^{3/8}\ HV^{1/2}}{D_C}} \qquad \text{[86] (5.5)}$$

## 5.8 Correlation of the abrasive wear resistance to mechanical properties using semi-empirical models

The wear resistance of most cermet composites is related to their hardness and fracture toughness as can be seen from most abrasive wear models (Table 5.3). The product of the hardness and fracture toughness ($K_{IC}^{a}.HV^{b}$) was proven to be related to the resistance to material removal caused by plastic deformation and fragmentation [85]–[88], [156], [157]. From Equation 5.6 and Figure 5.5a it is observed that the abrasive wear resistance increases nearly linear with such product in agreement with earlier works [156], [158]. This confirms the well-known tribology principle that an optimum balance must be reached to avoid too hard or too brittle material behavior.

$$\boldsymbol{R = \frac{1}{Q} = K.K_{IC}^{a}.HV^{b}} \qquad \text{[85]–[89], [157], [158] (5.6)}$$

Where R is the abrasion wear resistance; K is the wear coefficient; $K_{IC}$ is the fracture toughness; HV is the hardness; and a, b are the exponents. Table 5.2 shows the different models relating the hardness (HV), the fracture toughness ($K_{IC}$) and the abrasive wear resistance for various materials.

However, as seen in Figure 5.5a, while existing models (1 to 15 in Table 5.3) seem unanimous in the value of the hardness exponent b = 1/2, they have so far yielded different values for the fracture toughness exponent a, making them materials and test conditions dependent [148]. As such, existing model approaches do not allow generalization in order to predict the wear resistance of novel materials.

According to literature [87], the discrepancies in the a and b exponents is due to the fact that brittle materials such as ceramics are more sensitive to changes in fracture toughness [159] yielding a higher fracture toughness exponent a = 3/4. In contrast, more ductile materials such as cermets are less sensitive to relatively small changes in fracture toughness yielding a lower exponent a = 3/8. In agreement with this argumentation, a similar correlation developed in this study using the nonlinear optimization toolbox in Matlab yielded exponents a = 3/8 and b = 3/4 (16 to 19 in Table 5.2). The higher b exponent determined in this work indicates that the fabricated cermet composites with 50 wt.% steel matrix are considerably tough making the wear resistance even less sensitive to changes in toughness (low a value) and more sensitive to the hardness (high b value).

**Table 5.2: Different models relating the hardness HV, the fracture toughness $K_{IC}$ and the abrasive wear resistance R for various materials.**

| No. | Ref. | Materials | Equations |
|---|---|---|---|
| 1 | [86] | WC-6Co | $R = K.K_{IC}^{3/8}.HV^{1/2}$ |
| 2 | [86] | WC-6Co | |
| 3 | [86] | WC-6Co | |
| 4 | [86] | WC-12Co | |
| 5 | [86] | WC-12Co | |
| 6 | [86] | WC-12Co | |
| 7 | [87] | WC-6Co | |
| 8 | [87] | WC-6Co | |
| 9 | [87] | WC-6Co | |
| 10 | [87] | WC-6Co | |
| 11 | [87] | Tool steel | |
| 12 | [87] | $Al_2O_3$ | $R = K.K_{IC}^{3/4}.HV^{1/2}$ |
| 13 | [87] | $Al_2O_3$-30 TiC | |
| 14 | [87] | $Si_3N_4$ | |
| 15 | [87] | $Si_3N_4$-30 TiC | |
| 16 | Current study | SET1B (SS316L-50 wt. % $Al_2O_3$) | $R = K.K_{IC}^{3/8}.HV^{3/4}$ |
| 17 | | SET2A (SS316L-50 wt. % $Al_2O_3$) | |
| 18 | | SET2B (SS316L-50 wt. % $Al_2O_3$) | |
| 19 | | SET2C (SS316L-50 wt. % $Al_2O_3$) | |

Waynes et al. [86] noted that the models could be more accurate if microstructure parameters are considered in the abrasion parameter calculation. Accordingly, they added the grain or strengthening particle size as seen in Equation 5.7 and in Figure 5.5b.

$$\boldsymbol{R = \frac{1}{Q} = K.AP = K\ \frac{K_{IC}^{3/8} H^{1/2}}{D_C}} \qquad (2.6; 5.7)$$

Where R is the abrasion wear resistance; K is the wear resistance coefficient (proportionality constant); AP is the abrasion parameter; $K_{IC}$ is the fracture toughness; H is the hardness; and $D_C$ is the reinforcement particle size.

However, Figure 5.5b also shows a lack of consistency in the way the model describes Wayne's data and the composite wear resistance data generated in the current study (resulting different slopes). Therefore, as discussed earlier in subsection 5.4, the porosity P is considered as further microstructure parameter in this study as shown in Equation 5.8 and Figure 5.5c. As can be seen, Figure 5.5c shows a better consistency in modeling both sets of data, opening the possibility of interpolation to predict further data sets. The porosity exponent 11 and the particle size exponent 1/8 were also determined using the optimization toolbox in Matlab.

$$\boldsymbol{R = \frac{1}{Q} = K.AP = K\ \frac{K_{IC}^{3/8}\ HV^{3/4}\,(1-P)^{11}}{D_C^{1/8}}} \qquad (5.8)$$

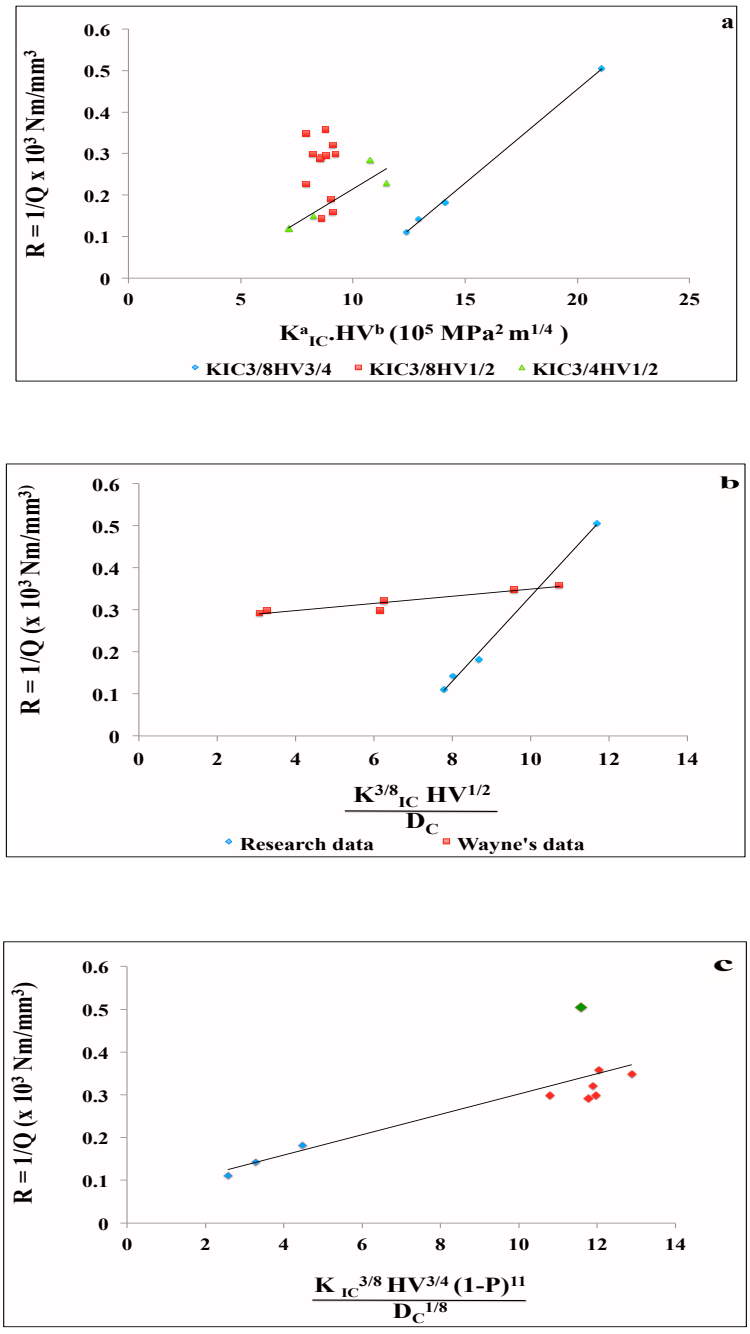


**Figure 5.5: Abrasion resistance as a function of AP: a) AP as calculated using only $K_{IC}$ and HV in different literature approaches; b) AP as calculated using the Wayne's model, Wayne's data and the wear data from this study; c) AP as calculated using the new model proposed in this study, Wayne's data and the wear data from this study.**

In addition to microstructure and mechanical properties, the wear resistance is known to also strongly depend on wear conditions. Therefore, a further improvement step was undertaken in this study by incorporating test conditions in the abrasive wear resistance calculation as shown in Equation 5.9 and Figure 5.6 [160].

$$\boldsymbol{R_C = \frac{1}{Q}\left(\frac{H_a}{H_c}\right)^{4/5} A_p{}^{1/8}\ V^{3/8}} \tag{5.9}$$

Where $R_C$ is the corrected abrasive wear resistance; Q is the specific wear rate; $H_a/H_c$ is the hardness ratio with $H_a$ the abrasive hardness and $H_c$ the composite hardness; $A_p$ is the abrasive grits size and V is the sliding speed or velocity.

The objective of the correction is to obtain a corrected wear resistance $R_C$ that is characteristic of the individual composites and is substantially independent of the test conditions [160]. This correction was generated using the optimization toolbox in Matlab as well and can be intuitively understood as follows. First, the ratio of abrasive particle hardness -to- composite hardness ($H_a/H_c$) can be expected to substantially affect the wear resistance. Harder abrasive particles (higher $H_a/H_c$ ratio) indent into the composite surface easier causing more rapid composite wear and leading to lower wear resistance [53], [84], [161]–[163]. Second, larger abrasive particles (larger $A_p$) are known to lead to deeper plug-in and correspondingly faster wear resulting in lower composite wear resistance [131], [164]–[167]. Finally, higher sliding speeds V can lead to stronger heating in the used test conditions of dry wear. Stronger heat input can soften materials making them more vulnerable to abrasive wear [168]. The result of the correction is a further improvement of the model. The model improvement achieved through the correction is particularly evident in the data point highlighted green and circled in Figure 5.5c that falls closer to the model

line in Figure 5.6.

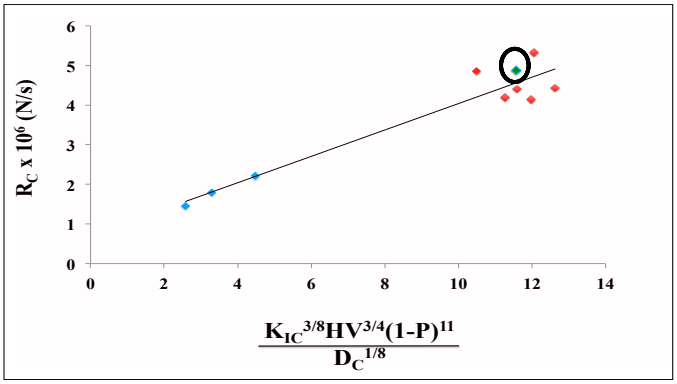


**Figure 5.6: Corrected abrasion wear resistance as a function of the abrasion parameter using Wayne's data and the wear resistance results from this study.**

The adequacy of the model is assessed using the coefficient of correlation r [169] for all fabricated composites. For the proposed model, r is found to be 0.99 after AP and $R_C$ corrections, which is close to the ideal value of 1.0 indicating a high degree of agreement between the predicted and the experimental data. Thus, the proposed model can be used to assess and evaluate the abrasive wear resistance (dry sliding wear) of SS316L-$Al_2O_3$ composites and probably other cermets.

To verify the generalization capacity of the above discussed model improvements, further literature [60], [86], [88], [170], [171] data, as shown in Table 5.3 and Figures 5.7a to 5.7c were used. It shall be noted that it was necessary to include fretting block-on-ring and slurry erosion test data due to the lack of literature publications providing further pin-on-disc wear data together with all the materials properties and test conditions required for the improved models. This led to substantially poor model performance prior to wear resistance correction.

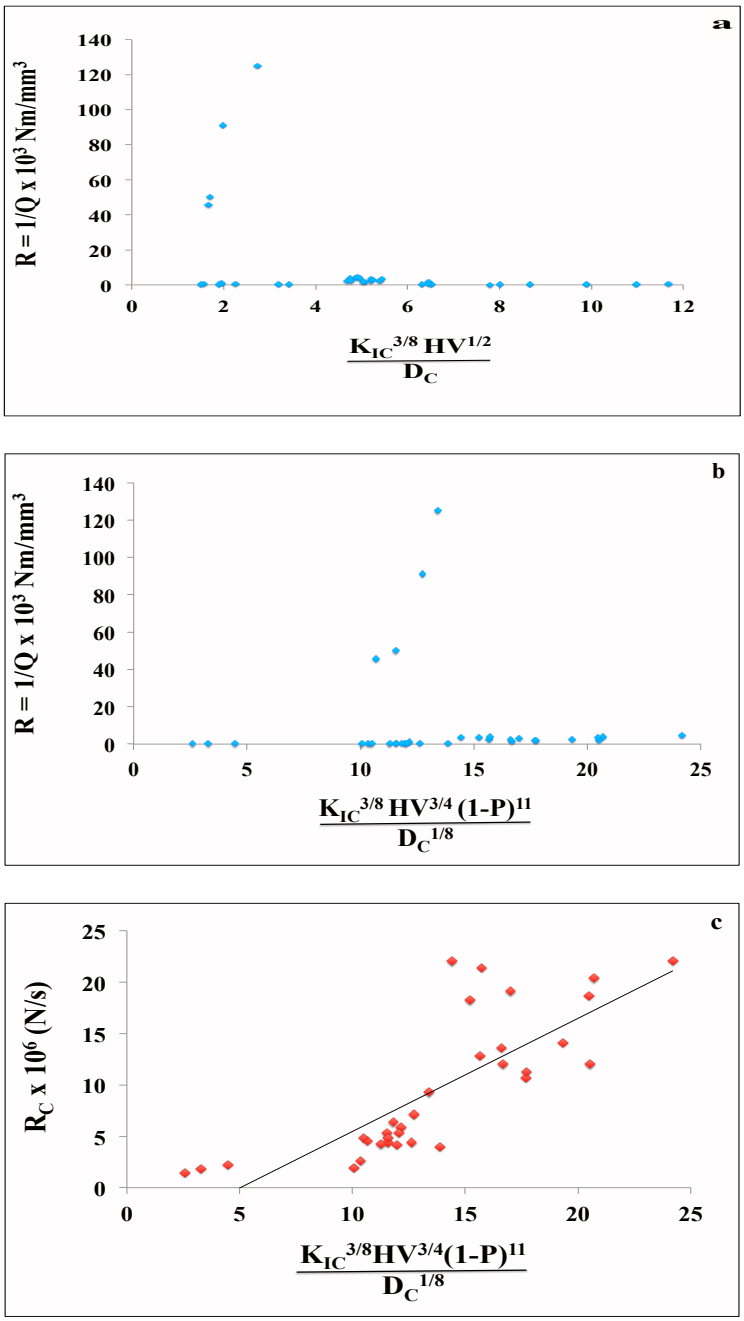


**Figure 5.7: Abrasive wear resistance as a function of AP for literature data and the wear resistance results from this study: a) AP calculated using Wayne's model; b) After porosity correction of AP; c) After the wear resistance correction to eliminate the effect of major test conditions.**

Despite the inclusion of microstructure parameters ($D_C$ and porosity) in the abrasive wear parameter AP calculation as can be seen in Figures 5.7a and 5.7b. However, the wear resistance correction through incorporation of the different test conditions produced a useful correlation despite the substantially dissimilar test conditions as seen in Figure 5.7c.

**Table 5.3: Wear testing conditions for all data**

| No. | Ref. | Materials | Testing conditions | Wear tester |
|---|---|---|---|---|
| 1 | Current study | SET1B (SS316L-50 wt. % $Al_2O_3$) | Dry | Pin-on-disk |
| 2 | | SET2A (SS316L-50 wt. % $Al_2O_3$) | Dry | Pin-on-disk |
| 3 | | SET2B (SS316L-50 wt. % $Al_2O_3$) | Dry | Pin-on-disk |
| 4 | | SET2C (SS316L-50 wt. % $Al_2O_3$) | Dry | Pin-on-disk |
| 5 | [86] | WC-6Co | Dry | Pin-on-disk |
| 6 | [86] | WC-6Co | Dry | Pin-on-disk |
| 7 | [86] | WC-6Co | Dry | Pin-on-disk |
| 8 | [86] | WC-12Co | Dry | Pin-on-disk |
| 9 | [86] | WC-12Co | Dry | Pin-on-disk |
| 10 | [86] | WC-12Co | Dry | Pin-on-disk |
| 11 | [60] | WC-6Co | Wet (Slurry) | Block-on-ring |
| 12 | [60] | WC-15Co | Wet (Slurry) | Block-on-ring |
| 13 | [60] | $Cr_3C_2$-10Ni | Wet (Slurry) | Block-on-ring |
| 14 | [60] | $Cr_3C_2$-20Ni | Wet (Slurry) | Block-on-ring |
| 15 | [60] | $Cr_3C_2$-30Ni | Wet (Slurry) | Block-on-ring |
| 16 | [170] | TiC-20NiMo (4:1)* | Wet (Slurry) | Block-on-ring |
| 17 | [170] | TiC-20NiMo (2:1)* | Wet (Slurry) | Block-on-ring |
| 18 | [170] | TiC-20NiMo (1:1)* | Wet (Slurry) | Block-on-ring |
| 19 | [170] | TiC-30NiMo (4:1)* | Wet (Slurry) | Block-on-ring |
| 20 | [170] | TiC-30NiMo (2:1)* | Wet (Slurry) | Block-on-ring |
| 21 | [170] | TiC-30NiMo (1:1)* | Wet (Slurry) | Block-on-ring |
| 22 | [170] | TiC-40NiMo (4:1)* | Wet (Slurry) | Block-on-ring |
| 23 | [170] | TiC-40NiMo (2:1)* | Wet (Slurry) | Block-on-ring |
| 24 | [170] | TiC-40NiMo (1:1)* | Wet (Slurry) | Block-on-ring |
| 25 | [170] | TiC-50NiMo (4:1)* | Wet (Slurry) | Block-on-ring |
| 26 | [170] | TiC-50NiMo (2:1)* | Wet (Slurry) | Block-on-ring |
| 27 | [170] | TiC-50NiMo (1:1)* | Wet (Slurry) | Block-on-ring |
| 28 | [88] | (W, Ti)-20Co (solid solution powder) ** | Fretting | Block-on-ring |
| 29 | [88] | (W,Ti)-20Co *** | Fretting | Block-on-ring |
| 30 | [88] | (W,Ti)-20Co **** | Fretting | Block-on-ring |
| 31 | [88] | (W,Ti)-20Co (premixed powder) ***** | Fretting | Block-on-ring |
| 32 | [167] | $Cr_3C_2$-10Ni | Wet (Slurry) | Block-on-ring |
| 33 | [167] | $Cr_3C_2$-20Ni | Wet (Slurry) | Block-on-ring |

Sintering conditions:
*(x,y) ratio of Ni to Mo
** 1500 ºC, 1hr.
*** 1450 ºC, 1hr and 1500 ºC, 1hr.
**** 1400 ºC, 1hr; 1450 ºC, 1hr and 1500 ºC, 1hr.
***** 1500 ºC, 1hr.

# 6 CONCLUSIONS

SS316L-$Al_2O_3$ composites were investigated for improved wear resistance. Samples were fabricated using the powder metallurgy (PM) route. Four sets of mechanical alloying parameters, different compaction pressures and two sets of sintering conditions were studied. The wear rates were compared to those of commercial 90WC-Co, commercial SS316 and unreinforced SS316L manufactured under the same conditions as the SS316L-$Al_2O_3$ composites. The following conclusions can be drawn at this stage:

- The lower milling speed of 720 rpm combined with a longer milling duration of 30 hrs is more appropriate for the mechanical alloying of SS316L-$Al_2O_3$ composites as it yielded lower porosity, higher hardness, and higher wear resistance.
- The compaction pressure of 794.4 MPa yielded the highest density, hardness and wears resistance.
- The sintering temperature of 1400 °C, which is above the melting point of SS316L, led to liquid phase sintering. In addition, with the use of argon sintering environment, this temperature enhanced diffusion and produced good densification, hardness and wear resistance.
- The addition of 50 wt.% particles resulted in up to 7.4 times lower wear rate compared to the fabricated unreinforced SS316L. However, the commercial 90WC-Co composites showed about 6 times lower wear rate compared to the best SS316L-$Al_2O_3$ composite sample fabricated so far. This is thought to be primarily due to the higher WC ceramic content of 90 wt.% compared to the 50 wt.% $Al_2O_3$ particle content used in the present work. The remaining porosity found in the fabricated SS316L-$Al_2O_3$ composites is a further cause of their relatively poor wear

performance. Therefore, more efficient compaction methods such as HIP or hot pressing could allow further improvement.

- The addition of the porosity as a further microstructural parameter to the abrasion parameter (AP) led to a considerable improvement of the Wayne's model.
- A correction of the abrasive wear resistance parameter is introduced in which the effects of major test conditions, including the sliding velocity, the abrasive grit size and the abrasive particle-to-composite hardness ratio, are considerably eliminated. The corrected abrasive wear resistance proved to better characterize the individual composites.
- The coefficient of correlation of the proposed model including the porosity correction of the abrasion parameter and the test condition correction of the wear resistance was determined to be 0.91 for fabricated composites and Wayne's composites. This is close to the ideal value of 1 providing a high level of confidence, and opening the possibility of interpolation to predict the wear behavior of novel materials and the influence of wear conditions.

# 7 FUTURE WORK

The research investigation so far has successfully produced SS316L-$Al_2O_3$ composites with a ceramic particle size around 1 μm. A homogeneous microstructure and a uniform particle distribution were achieved. The new composites were proven to possess higher wear resistance compared to the fabricated unreinforced SS316L and commercial SS316. However, the wear rate was observed to be higher as compared to commercial 90WC-Co composites.

Therefore, a wide scope of future researches can be envisaged with the goal of further improving the microstructure, the density and the mechanical properties of Steel-$Al_2O_3$ composites for wear applications. Few recommendations include:

- The ball milling process can be further optimized in order to achieve nano-size ceramic reinforcement particles. Nanostructured cermets were proven to potentially lead to improved wear properties, particularly in fine abrasive and sliding wear applications [96], [172], [173].
- Also, hot pressing or hot isostatic pressing (HIP) shall be considered in order to further improve the densification process and sintering. The composites fabricated in this study using cold pressing followed by pressureless sintering contained porosities of 5 % or higher. Eliminating porosity and achieving densities close to the theoretical density can be expected to substantially improve the hardness, toughness and wear resistance of the composites.
- Although the models achieved useful correlations after corrections of both the abrasion parameter and the wear resistance, a more advanced consideration of the test set-up is recommended as it could produce even better model performance. In

fact, the current model does not make any specific differentiation between test set-ups [160]. For instance, slurry erosion versus pin-on-disk abrasive wear testing. It is known that loose abrasives such as in erosion testing are less aggressive and can be expected to produce lower wear rates than bounded abrasives such as in the case of pin-on-disk abrasive wear tests.

## SCIENTIFIC CONTRIBUTIONS

The following contributions had been made in this study:

1. SS316L-$Al_2O_3$ composite samples were successfully fabricated. The relatively low costs, availability and known excellent mechanical properties of steels and alumina make them outstanding candidates for fabricating composites for highly demanding wear applications. Presently, WC-Co composites are widely used for wear applications. However, WC-Co composites are known to have a low impact resistance during operation.
2. The Fabrication parameter effect was studied with respect to the mechanical properties; the microstructural parameters and the abrasive wear behaviour under dry sliding condition for SS316L-$Al_2O_3$ composites.
3. For the fracture toughness, various indentation fracture toughness equations were studied and the Evans and Wilshaw (for Palmqvist cracks) was found to be most accurate for SS316L-$Al_2O_3$ composites in this study.
4. A model was developed to relating the mechanical properties and microstructure parameters in the assessment of the abrasion parameter of cermets by introducing the porosity as further microstructural parameter.
5. Furthermore, a model was proposed for correcting the abrasive wear resistance by eliminating the test conditions (the hardness ratio, sliding velocity and abrasive grits size). The model was validated with multiple sets of data from literature generated under different wear testing conditions. Therefore, the proposed model opens an avenue for interpolation allowing prediction or

assessing the wear behaviour of novel materials or the effect of new testing conditions.

## Scientific Publications

Published Journal Publication

1. Kuforiji, C., and Nganbe, M., 'Modelling the effect of microstructure, properties and abrasion conditions of the wear resistance of SS316L-$Al_2O_3$ composites', Journal of Tribology International, vol. 111, pp. 100-106, 2017.

International Conference Proceeding

2. Kuforiji, C., and Nganbe, M., 'Fabrication and Characterization of SS316L-$Al_2O_3$ Composites for Wear Applications', ICANM 2015: International Conference and Exhibition on Advanced and Nano Materials, Ottawa, Ontario, Canada, 2015, 9 pages.

Abstract

3. Kuforiji, C., and Nganbe, M., 'Wear Assessment of SS316L-$Al_2O_3$ Composites For Heavy Wear Applications' ICANM 2016: International Conference on Advanced Materials and Nanotechnology, Bangkok, Thailand, 2016.

# 8 REFERENCE


[1] M. Petrica, E. Badisch, and T. Peinsitt, 'Abrasive Wear Mechanisms and their Relation to Rock Properties', *Wear*, vol. 308, no. 1–2, pp. 86–94, 2013.

[2] K. Zum Gahr, 'Microstructure and Wear of Materials', *Amsterdam, The Netherlands, Elsevier Sci. Publishers B.V.,* vol. 10, pp. 1–116, 1987.

[3] G. Stachowiak and A. Batchelor, '11 - Abrasive, Erosive and Cavitation Wear', *Eng. Tribol. Third Ed.*, pp. 501–551, 2006.

[4] J. Pirso, S. Letunovitš, and M. Viljus, 'Friction and Wear Behaviour of Cemented Carbides', *Wear*, vol. 257, no. 3–4, pp. 257–265, 2004.

[5] R. German, 'Powder Metallurgy Science', Princeton, NJ, USA: Metal Powder Industries Federation, pp. 425-472, 1994.

[6] M. Nganbe, T. Khan, and L. Glenesk, 'High Wear Resistant HVOF Coatings for Use in the Oil and Sands Industry', *Symposium on Materials Technology in Mechanical Engineering.*, Calgary, Alberta, 2006.

[7] G. Gille, K. Dreyer, H. Van Den Berg, J. Schmidt, T. Gestrich, and G. Leitner, 'Submicron and Ultrafine Grained Hardmetals for Microdrills and Metal Cutting Inserts', *Int. J. Refract. Met. Hard Mater*, vol. 20, pp. 3–22, 2002.

[8] K. Konopka, 'Novel Ceramic-Metal Composites with Metal Phase from Micro to Nanosize', *Solid State Phenom.*, vol. 101, pp. 139–142, 2004.

[9] E. Pagounis and V. Lindroos, 'Processing and Properties of Particulate Reinforced Steel Matrix Composites', *Mater. Sci. Eng. A (Structural Mater. Prop. Microstruct. Process.*, vol. A246, no. 1–2, pp. 221–234, 1998.

[10] V. Rajkovic, D. Bozic, and M. Jovanovic, 'Properties of Copper Matrix Reinforced with Nano- and Micro-Sized $Al_2O_3$ Particles', *J. Alloys Compd.*, vol. 459, no. 1–2, pp. 177–184, 2008.

[11] A. Aksenov, M. Samoshina, and N. Belov, 'The Structure and Properties of Dispersion-Strengthened Mechanically-Alloyed Composite Materials Based on Aluminum Alloys', *Mater. Sci. Forum*, vol. 28, pp. 1303–1308, 2004.

[12] R. Siegel, 'Synthesis and Properties of Nanophase Materials', *EMRS 1992 Fall Meeting, Symposium C: Nanophase Materials*, vol. A168, no. 2, pp. 189–197, 1993.

[13] H. Mahboob, S. Sajjadi, and S. Zebarjad, 'Influence of Nanosized $Al_2O_3$ Weight Percentage on Microstructure and Mechanical Properties of Al-Matrix Nanocomposite', *Powder Metall.*, vol. 54, no. 2, pp. 148–152, 2011.

[14] C. Suryanarayana, 'Mechanical Alloying and Milling', *Progress in Mater. Sci.*, vol. 46, pp. 1-184, 2001.

[15] B. Murty and S. Ranganathan, 'Novel Materials Synthesis by Mechanical Alloying/Milling', *Int. Mater. Rev.*, vol. 43, no. 3, pp. 101–141, 1998.

[16] H. Gleiter, 'Nanostructure Materials: Basic Concepts and Microstructure', *Acta Mater.*, vol. 48, pp. 1–29, 2000.

[17] N. Tao, J. Lu, and K. Lu, 'Surface Nanocrystallization by Surface Mechanical Attrition Treatment', *Mater. Sci. Forum*, vol. 79, pp. 91–108, 2008.

[18] S. Lal and G. Upadhyaya, 'Effect of $Y_2O_3$ Addition and Sintering Period on the Properties of 316L Austenitic Stainless Steel', *J. Mater. Sci.*, vol. 6, pp. 761–764, 1987.

[19] C. Onuoha, G. Kipouros, Z. Farhat, and K. Plucknett, 'The Reciprocating Wear Behaviour of TiC–304L Stainless Steel Composites Prepared by Melt Infiltration', *Wear*, vol. 303, no. 1–2, pp. 321–333, 2013.

[20] J. Miranda-Hernández, E. Refugio-García, E. Térres-Rojas, and E. Rocha-Rangel, 'Titanium Effect on Microstructure and Fracture Toughness of $Al_2O_3$-Based Composites', *Mater. Sci. Forum*, vol. 691, pp. 32–36, 2011.

[21] R. Tongsri, C. Mateepithukgharm, T. Piyarattanatrai and P. Wangyao, 'Effect of Powder Mixture Conditions on Mechanical Properties of Sintered $Al_2O_3$-SS316L Composite under Vacuum Atmosphere', *J. Met. Mater. Miner.*, vol. 17, no. 1, pp. 81–85, 2007.

[22] T. Yodkaew *et al.*, 'Effect of Non- Reactive Hard Particles on Sintered Fe Material', *Songklanakarin J. Sci. Technol.*, vol. 31, no. 5, pp. 555–559, 2009.

[23] R. German, 'Powder Metallurgy of Iron and Steel', New York: New York Wiley, pp. 175–188, 1998.

[24] M. Samoshina, A. Aksenov, and E. Kaevitser, 'Structure and Properties of Mechanically Alloyed Composite Materials from Hard Recycling Scrap of Al Alloys', *Rev. Adv. Mater. Sci*, vol. 18, pp. 305–311, 2008.

[25] N. Eigen, T. Klassen, E. Aust, R. Bormann, and F. Gärtner, 'Production of Nanocrystalline Cermet Thermal Spray Powders for Wear Resistant Coatings by High-Energy Milling', *Mater. Sci. Eng. A*, vol. 356, no. 1, pp. 114–121, 2003.

[26] Z. Zongyin, 'Processing of Nanostructured WC-Co Powders and Sintered Steels', 2003.

[27] C. Santos Torres and L. Schaeffer, 'Effect of High Energy Milling on the Microstruture and Properties of WC-Ni Composite', *Mater. Res.*, vol. 13, no. 3, pp. 293–298, 2010.

[28] M. Chmielewski, K. Pietrzak, and W. Włosiński, 'Properties of Sintered $Al_2O_3$-Cr Composites Depending on the Method of Preparation of the Powder Mixture', *Sci. Sinter.*, vol. 38, no. 3, pp. 231–238, 2006.

[29] O. Coovattanachai *et al.*, 'Analysis of Compaction and Sintering of Stainless Steel Powders', *Chiang Mai J. Sci.*, vol. 33, no. 2, pp. 293–300, 2006.

[30] S. Clyens and W. Johnson, 'The Dynamic Compaction of Powdered Materials', *Mater. Sci. Eng.*, vol. 30, no. 2, pp. 121–139, 1977.

[31] A. Akisanya, A. Cocks, and N. Fleck, 'Hydrostatic Compaction of Cylindrical Particles', *J. Mech. Phys. Solids*, vol. 42, no. 7, pp. 1067–1085, 1994.

[32] B. Briscoe and N. Özkan, 'Compaction Behaviour of Agglomerated Alumina Powders', *Powder Technol.*, vol. 90, no. 3, pp. 195–203, 1997.

[33] J. Wang, X. Qu, H. Yin, M. Yi, and X. Yuan, 'High Velocity Compaction of Ferrous Powder', *Powder Technol.*, vol. 192, no. 1, pp. 131–136, 2009.

[34] A. Cocks, 'Constitutive Modelling of Powder Compaction and Sintering', *Prog. Mater. Sci.*, vol. 46, no. 3–4, pp. 201–229, 2001.

[35] C. Martin, D. Bouvard, and S. Shima, 'Study of Particle Rearrangement during Powder Compaction by the Discrete Element Method', *J. Mech. Phys. Solids*, vol. 51, no. 4, pp. 667–693, 2003.

[36] G. Upadhyaya, 'Powder Metallurgy Technology', Cambridge International Science

Publishing, pp. 1-170, 2002.

[37] Z. Fang and H. Wang, '13 - Sintering of Ultrafine and Nanosized Ceramic and Metallic Particles', *Ceram. Nanocomposites*, pp. 431–473, 2013.

[38] S. Panda, V. Singh, A. Upadhyaya, and D. Agrawal, 'Effect of Conventional and Microwave Sintering on the Properties of Yttria Alumina Garnet-Dispersed Austenitic Stainless Steel', *Metall. Mater. Trans. A Phys. Metall. Mater. Sci.*, vol. 37, no. 7, pp. 2253–2264, 2006.

[39] D. Dyke and H. Ambs, 'Stainless Steel Powder Metallurgy', pp. 123–144, 1983.

[40] G. Lei, R. German, and H. Nayar, 'Influence of Sintering Variables on Corrosion Resistance of 316L Stainless Steel', *Powder Metall. Int.*, vol. 15, no. 2, pp. 70–76, 1983.

[41] H. Nayar, R. German, and W. Johnson, 'The Effect of Sintering on the Corrosion Resistance of 316L Stainless Steel', *Prog. Powder Metall.*, vol. 37, pp. 255–265, 1981.

[42] N. Shaw and R. Honeycombe, 'Some Factors Influencing the Sintering Behavior of Austenitic Stainless Steel Powders', *Powder Metall.*, vol. 20, no. 4, pp. 191–198, 1977.

[43] T. Yotkeaw, R. Krataitong, M. Morakotjinda, A. Daraphan, N. Tosangthum, and O. Coovattanachai, 'Reinforcement of P/M 316L by $Al_2O_3$ Particles', Pathumthani: National Metal and Materials Technology Centre, M08, pp. 1–3, 2006.

[44] W. Stichel, 'ASM Speciality Handbook: Stainless Steels', *ASM International, Materials Park, Ohio, USA, 1994.*

[45] I. Hussainova, I. Jasiuk, M. Sardela, and M. Antonov, ‘Micromechanical Properties and Erosive Wear Performance of Chromium Carbide Based Cermets’, *Wear*, vol. 267, no. 1, pp. 152–159, 2009.

[46] I. Uygur, ‘Microstructure and Wear Properties of AISI 1038H Steel Weldments’, *Ind. Lubr. Tribol.*, vol. 58, no. 6, pp. 303–311, 2006.

[47] T. Eyre, ‘The Mechanisms of Wear’, *Tribol. Int.*, vol. 11, no. 2, pp. 91–96, 1978.

[48] A. Zmitrowicz, ‘Wear Patterns and Laws of Wear–A Review’, *J. Theor. Appl. Mech.*, vol. 44, no. 2, pp. 219–253, 2006.

[49] J. Davis, ‘Surface Engineering for Corrosion and Wear Resistance’, Materials Park, Ohio; OH: Woodhead Publishing, 2001.

[50] H. Ameen, K. Hassan, and E. Mubarak, ‘Effect of Loads, Sliding Speeds and Times on the Wear Rate for Different Materials’, *Am. J. Sci. Ind. Res.*, vol. 2, pp. 99–106, 2011.

[51] G. Stachowiak and A. Batchelor, ‘Preface’, in *Engineering Tribology*, G. W. S. W. Batchelor, Ed. Burlington: Butterworth-Heinemann, 1993, pp. 613–635.

[52] N. DiMatteo and S. Lampman, ‘ASM Handbook, Volume 19: Fatigue and Fracture’, vol. 19, p. 1057, 1996.

[53] T. Adeva Rodil, ‘Edge Effect on Abrasive Wear Mechanisms and Wear Resistance in WC-6wt.% Co Hardmetals’, 2006.

[54] K. Grigoroudis, ‘A Study of the Wear Process Related to Twin-Screw Extruders’, Cranfield University, 1996.

[55] P. Shipway and J. Hogg, ‘Wear of Bulk Ceramics in Micro-Scale Abrasion—The

Role of Abrasive Shape and Hardness and its Relevance to Testing of Ceramic Coatings', *Wear*, vol. 263, no. 7, pp. 887–895, 2007.

[56] I. Kovaříková, B. Szewczyková, and P. Blaškoviš, 'Study and Characteristic of Abrasive Wear Mechanisms', *Mater. Sci. Technol.*, pp. 1335–9053, 2015.

[57] S. Nahvi, 'Abrasive Wear Behaviour of Steels and Advanced HVOF-Sprayed WC-M Coatings', PhD thesis, University of Nottingham, 2011.

[58] I. Hutchings, 'Wear-Resistant Materials: Into the Next Century', *Mater. Sci. Eng. A*, vol. 184, no. 2, pp. 185–195, 1994.

[59] S. Nahvi, P. Shipway, and D. McCartney, 'Particle Motion and Modes of Wear in the Dry Sand–Rubber Wheel Abrasion Test', *ICAP 2008*, vol. 267, no. 11, pp. 2083–2091, 2009.

[60] J. Pirso, M. Viljus, S. Letunovitš, K. Juhani, and R. Joost, 'Three-Body Abrasive Wear of Cermets', *Wear*, vol. 271, no. 11–12, pp. 2868–2878, 2011.

[61] H. Engqvist and N. Axén, 'Abrasion of Cemented Carbides by Small Grits', *Tribol. Int.*, vol. 32, no. 9, pp. 527–534, 1999.

[62] S. Tjong and K. Lau, 'Abrasion Resistance of Stainless-Steel Composites Reinforced with Hard $TiB_2$ Particles', *Compos. Sci. Technol.*, vol. 60, no. 8, pp. 1141–1146, 2000.

[63] S. Vettivel, N. Selvakumar, R. Narayanasamy, and N. Leema, 'Numerical Modelling, Prediction of Cu-W Nano Powder Composite in Dry Sliding Wear Condition using Response Surface Methodology', *Mater. Des.*, vol. 50, pp. 977–996, 2013.

[64] N. Radhika, R. Subramanian, S. Prasat, and B. Anandavel, 'Dry Sliding Wear

Behaviour of Aluminium/Alumina/Graphite Hybrid Metal Matrix Composites', *Ind. Lubr. Tribol.*, vol. 64, no. 6, pp. 359–366, 2012.

[65] M. Imbaby and K. Jiang, 'Net Shape Fabrication of Stainless Steel–Alumina Composite Micro Parts', *J. Micromechanics Microengineering*, vol. 19, no. 4, pp. 360–365, 2009.

[66] H. Gulsoy, T. Baykara, and S. Ozbek, 'Injection Moulding of 316L Stainless Steels Reinforced with Nanosize Alumina Particles', *Powder Metall.*, vol. 54, no. 3, pp. 360–365, 2011.

[67] M. Vardavoulias, M. Jeandin, F. Velasco, and J. Torralba, 'Dry Sliding Wear Mechanism for P/M Austenitic Stainless Steels and their Composites Containing $Al_2O_3$ and $Y_2O_3$ Particles', *Tribol. Int.*, vol. 29, no. 6, pp. 499–506, 1996.

[68] E. Rocha-Rangel, 'Fracture Toughness Determinations by Means of Indentation Fracture', *Intech Open Access Publisher*, pp. 1–19, 2011.

[69] K. Zum Gahr, 'Wear by Hard Particles', *Tribol. Int.*, vol. 31, no. 10, pp. 587–596, 1998.

[70] J. Hu, D. Li, and R. Llewellyn, 'Computational Investigation of Microstructural Effects on Abrasive Wear Of Composite Materials', *15th Int. Conf. Wear Mater.*, vol. 259, no. 1–6, pp. 6–17, 2005.

[71] I. Hutchings, 'Wear by Particulates', *Chem. Eng. Sci.*, vol. 42, no. 4, pp. 869–878, 1987.

[72] S. Das, D. Mondal, and G. Dixit, 'Correlation of Abrasive Wear with Microstructure and Mechanical Properties of Pressure Die-Cast Aluminum Hard-Particle

Composite', *Metall. Mater. Trans. A*, vol. 32, no. 3, pp. 633–642, 2001.

[73] E. Zdravecká, J. Tkácová, and M. Ondác, 'Effect of Microstructure Factors on Abrasion Resistance of High-Strength Steels', *Czech Acad. Agric. Sci.*, vol. 60, no. 3, pp. 115–120, 2014.

[74] J. Yeomans, 'Ductile Particle Ceramic Matrix Composites', *J. Eur. Ceram. Soc.*, vol. 28, pp. 1543–1550, 2008.

[75] G. Lee, C. Dharan, and R. Ritchie, 'A Physically-Based Abrasive Wear Model for Composite Materials', *Wear*, vol. 252, no. 3–4, pp. 322–331, 2002.

[76] C. Allen, M. Sheen, J. Williams, and V. Pugsley, 'The Wear of Ultrafine WC–Co Hard Metals', *Wear*, vol. 250, no. 1–12, pp. 604–610, 2001.

[77] S. Prasad and P. Calvert, 'Abrasive Wear of Particle-Filled Polymers', *J. Mater. Sci.*, vol. 15, no. 7, pp. 1746–1754, 1980.

[78] J. Williams, 'Wear Modelling: Analytical, Computational and Mapping: A Continuum Mechanics Approach', *12th Int. Conf. Wear Mater.*, vol. 225–229, no. 1, pp. 1–17, 1999.

[79] H. Fallahdoost, H. Khorsand, R. Eslami-Farsani, and E. Ganjeh, 'On the Tribological Behavior of Nanoalumina Reinforced Low Alloy Sintered Steel', *Mater. Des.*, vol. 57, no. 0, pp. 60–66, 2014.

[80] W. Simm and S. Freti, 'Abrasive Wear of Multiphase Materials', *Wear*, vol. 129, no. 1, pp. 105–121, 1989.

[81] R. Colaço and R. Vilar, 'A Model for the Abrasive Wear of Metallic Matrix Particle-Reinforced Materials', *Wear*, vol. 254, no. 7–8, pp. 625–634, 2003.

[82] B. Bhushan, Principles and Applications of Tribology*, Second Edition*. New York: New York Wiley, pp. 474-475, 2013.

[83] M. Bingley and S. Schnee, 'A Study of the Mechanisms of Abrasive Wear for Ductile Metals under Wet and Dry Three-Body Conditions', *Wear*, vol. 258, no. 1, pp. 50–61, 2005.

[84] M. Moore and F. King, 'Abrasive Wear of Brittle Solids', *International Conference on Wear of Materials*, vol. 60, no. 1, pp. 123–140, 1980.

[85] D. Stewart, P. Shipway, and D. McCartney, 'Abrasive Wear Behaviour of Conventional and Nanocomposite HVOF-Sprayed WC–Co Coatings', *Wear*, vol. 225–229, no. 0, pp. 789–798, 1999.

[86] S. Wayne, J. Baldoni, and S. Buljan, 'Abrasion and Erosion of WC-Co with Controlled Microstructures', *Tribol. Trans.*, vol. 33, no. 4, pp. 611–617, 1990.

[87] J. Baldoni, S. Wayne, and S. Buljan, 'Cutting Tool Materials: Mechanical Properties—Wear-Resistance Relationships', *ASLE Trans.*, vol. 29, no. 3, pp. 347–352, 1986.

[88] S. Bodhak, B. Basu, T. Venkateswaran, W. Jo, K. Jung, and D. Kim, 'Mechanical and Fretting Wear Behavior of Novel (W, Ti) C–Co Cermets', *J. Am. Ceram. Soc.*, vol. 89, no. 5, pp. 1639–1651, 2006.

[89] L. Peng, J. Cao, K. Noda, and K. Han, 'Mechanical Properties of Ceramic-Metal Composites by Pressure Infiltration of Metal into Porous Ceramics', *Mater. Sci. Eng. A*, vol. 374, no. 1–2, pp. 1–9, 2004.

[90] N. Axén, A. Alahelisten, and S. Jacobson, 'Abrasive Wear of Alumina Fibre-

Reinforced Aluminium', *Wear*, vol. 173, no. 1–2, pp. 95–104, 1994.

[91] P. Kivikytö-Reponen, 'Correlation of Material Characteristics and Wear of Powder Metallurgical Metal Matrix Composites', Helsinki University of Technology, 2006.

[92] H. Li, S. Bhaduri, and J. Sekhar, 'Metal-Ceramic Composites Based on the Ti-B-Cu Porosity System', *Metall. Trans. Phys. Metall. Mater. Sci.*, vol. 23 A, no. 1, pp. 251–261, 1992.

[93] S. Monan, V. Prakash, and J. Pathak, 'Wear Characteristics of HSLA Steel', *J. Wear*, vol. 252, no. 1–2, pp. 16–25, 2002.

[94] H. Klaasen and J. Kübarsepp, 'Abrasive Wear Performance of Carbide Composites', *Wear*, vol. 261, no. 5–6, pp. 520–526, 2006.

[95] P. Shipway and J. Hogg, 'Dependence of Microscale Abrasion Mechanisms of WC-Co Hardmetals on Abrasive Type', *15th Int. Conf. Wear Mater.*, vol. 259, no. 1–6, pp. 44–51, 2005.

[96] K. Jia and T. Fischer, 'Abrasion Resistance of Nanostructured and Conventional Cemented Carbides', *Wear*, vol. 200, no. 1–2, pp. 206–214, Jan. 1996.

[97] M. Rodríguez, L. Gil, S. Camero, N. Fréty, Y. Santana, and J. Caro, 'Effects of the Dispersion Time on the Microstructure and Wear Resistance of WC/Co-Cnts HVOF Sprayed Coatings', *Surf. Coatings Technol.*, vol. 258, pp. 38–48, 2014.

[98] C. Bao, J. Xing, Y. Gao, and E. Wang, 'Wear Resistant of $Al_2O_3$/Heat-Resistant Steel at High Temperature', *3rd Int. Conf. High-Performance Ceram.*, vol. 280–283, pp. 1119–1122, 2005.

[99] G. Zhou and H. Ding, 'Wear Performance of Alumina-Reinforced Copper-Matrix

Composites Prepared by Powder Metallurgy', *Proc. Inst. Mech. Eng. Part J (J. Eng. Tribol.*, vol. 227, no. 9, pp. 1011–1017, 2013.

[100] P. Datta and G. Upadhyaya, 'Investigation of Sintered M2-5wt.% Cu Steels Containing $Al_2O_3$ Particles', *Met. Powder Rep.*, vol. 55, no. 12, pp. 28–32, 2000.

[101] M. Dewidar, 'Influence of Processing Parameters and Sintering Atmosphere on the Mechanical Properties and Microstructure of Porous 316L Stainless Steel for Possible Hard-Tissue Applications', *Int. J. Mech. Mechatronics Eng.*, vol. 12, no. 1, pp. 10–24.

[102] S. Shamsuddin, 'Characterization of Fe-Cr-$Al_2O_3$ Composites Fabricated by Powder Metallurgy Method with Varying Weight Percentage of Alumina', *J. Phys. Sci.*, vol. 19, no. 1, pp. 89–95, 2008.

[103] J. Auger, S. Saunier, and F. Valdivieso, 'Characterisation of Sintering of Alumina Matrix-Stainless Steel Dispersion Composite and Interaction between Chromium, Carbon and Alumina during Powder Metallurgy Process', *Powder Metall.*, vol. 54, no. 4, pp. 522–528, 2011.

[104] M. Rahimian, N. Parvin, and N. Ehsani, 'The Effect of Production Parameters on Microstructure and Wear Resistance of Powder Metallurgy Al–$Al_2O_3$ Composite', *Mater. Des.*, vol. 32, no. 2, pp. 1031–1038, 2011.

[105] D. Bhalla, D. Singh, S. Singh, and D. Seth, 'Material Processing Technology for Soft Ferrites Manufacturing', *Am. J. Mater. Sci.*, vol. 2, no. 6, pp. 165–170, 2012.

[106] F. Sergejev and M. Antonov, 'Comparative Study on Indentation Fracture Toughness Measurements of Cemented Carbides', *Proc. Est. Acad. Sci.*, vol. 12, no. 4, pp. 388–

398, 2006.

[107] M. Masanta, S. Shariff, and A. Roy Choudhury, 'Evaluation of Modulus of Elasticity, Nano-Hardness and Fracture Toughness of $TiB_2$–TiC–$Al_2O_3$ Composite Coating Developed by SHS and Laser Cladding', *Mater. Sci. Eng. A*, vol. 528, no. 16, pp. 5327–5335, 2011.

[108] K. Niihara, R. Morena, and D. Hasselman, 'Evaluation of $K_{Ic}$ of Brittle Solids by the Indentation Method with Low Crack to Indent Ratios', *J. Mater. Sci. Lett.*, vol. 1, pp. 13–16, 1982.

[109] J. Newkirk and J. Hawk, 'Abrasive Wear Properties of Cr–$Cr_3Si$ Composites', *13th Int. Conf. Wear Mater.*, vol. 251, no. 1–12, pp. 1361–1371, 2001.

[110] R. Bidulský, J. Bidulská, F. Arenas, and M. Grande, 'Wear Characteristics of Sintered Cermets', *High Temp. Mater. Process.*, vol. 31, no. 1, pp. 13–17, 2012.

[111] R. Roy, H. Guchhait, A. Chanda, D. Basu, and M. Mitra, 'Improved Sliding Wear-Resistance of Alumina with Sub-Micron Grain Size: A Comparison with Coarser Grained Material', *J. Eur. Ceram. Soc.*, vol. 27, no. 16, pp. 4737–4743, 2007.

[112] S. Mahathanabodee, T. Palathai, S. Raadnui, R. Tongsri, and N. Sombatsompop, 'Dry Sliding Wear Behavior of SS316L Composites Containing H-BN and $MoS_2$ Solid Lubricants', *Wear*, vol. 316, no. 1–2, pp. 37–48, 2014.

[113] S. Hewitt and K. Kibble, 'Effects of Ball Milling Time on the Synthesis and Consolidation of Nanostructured WC–Co Composites', *Int. J. Refract. Met. Hard Mater.*, vol. 27, no. 6, pp. 937–948, 2009.

[114] A. Fathy, F. Shehata, M. Abdelhameed, and M. Elmahdy, 'Compressive and Wear

Resistance of Nanometric Alumina Reinforced Copper Matrix Composites', *Sustain. Mater. Des. Appl.*, vol. 36, no. 0, pp. 100–107, 2012.

[115] B. Saha, V. Kumar, S. Joshi, A. Balakrishnan, and C. Martin, 'Investigation of Compaction Behavior of Alumina Nano Powder', *Powder Technol.*, vol. 224, no. 0, pp. 90–95, 2012.

[116] R. German, P. Suri, and S. Park, 'Review: Liquid phase sintering', *J. Mater. Sci.*, vol. 44, no. 1, pp. 1–39, 2009.

[117] K. Grilec, 'Hardness and Fracture Toughness of Alumina Ceramics', *12. Savjet. o Mater. Tehnol. trenju i trošenju*, 2007.

[118] R. Spiegler, S. Schmauder, and L. Sigl, 'Fracture Toughness Evaluation of WC–Co Alloys by Indentation Testing', *J. Hard Mater.*, vol. 1, no. 3, pp. 147–158, 1990.

[119] M. Rahimian, N. Ehsani, N. Parvin, and H. Baharvandi, 'The Effect of Sintering Temperature and the Amount of Reinforcement on the Properties of Al–$Al_2O_3$ Composite', *Mater. Des.*, vol. 30, no. 8, pp. 3333–3337, 2009.

[120] M. Rahimian, N. Parvin, and N. Ehsani, 'Investigation of Particle Size and Amount of Alumina on Microstructure and Mechanical Properties of Al Matrix Composite Made by Powder Metallurgy', *Mater. Sci. Eng. A*, vol. 527, no. 4–5, pp. 1031–1038, 2010.

[121] E. Haimi, M. Talvitie, E. Ristolainen, J. Kivilahti, and V. Lindroos, 'Characterisation of Interfacial Layer Between Nitrogen Alloyed Stainless Steel and Alumina in A Metal Matrix Composite', *Scr. Metall. Mater.*, vol. 30, no. 10, pp. 1333–1336, 1994.

[122] M. Dumovic, 'Repair and Maintenance Procedures for Heavy Machinery Components', *Weld. Innov.*, vol. 20, no. 1, pp. 1–5, 2003.

[123] P. Kulu, R. Tarbe, and A. Vallikivi, 'Abrasive Wear of Powder Materials and Coatings', *Mater.Sci.(Medziagotyra)*, vol. 11, pp. 1320–1392, 2005.

[124] F. Zok and C. Levi, 'Mechanical Properties of Porous-Matrix Ceramic Composites', *Adv. Eng. Mater.*, vol. 3, no. 1, pp. 15–23, 2001.

[125] D. Poquillon, J. Lemaitre, V. Baco-Carles, P. Tailhades, and J. Lacaze, 'Cold Compaction of Iron Powders—Relations between Powder Morphology and Mechanical Properties: Part I: Powder Preparation And Compaction', *Powder Technol.*, vol. 126, no. 1, pp. 65–74, 2002.

[126] M. Delavari, A. Salarvand, A. Rahi, and F. Shahri, 'The Effect of Powder Metallurgy Process Parameters on Mechanical Properties of Micro and Nano-Iron Powder', *Int. J. Eng. Sci. Technol.*, vol. 3, no. 9, pp. 86–94, 2011.

[127] N. Aqeeli, N. Saheb, T. Laoui, and K. Mohammad, 'The Synthesis of Nanostructured WC-Based Hardmetals using Mechanical Alloying and Their Direct Consolidation', *J. Nanomater.*, vol. 18, pp. 16, 2014.

[128] D. Kotecki and J. Ogborn, 'Abrasion Resistance of Iron-Based Hardfacing Alloys', *Weld. Journal- Weld. Res. Suppl.*, vol. 74, no. 8, pp. 269–278, 1995.

[129] R. German, 'Sintering Theory and Practice', *ISBN 0-471-05786-X.Wiley-VCH,* vol. 1, pp. 568, 1996.

[130] N. Axen and K. Zum Gahr, 'Abrasive Wear of TiC-Steel Composite Clad Layers on Tool Steel', *Wear*, vol. 157, no. 1, pp. 189–201, 1992.

[131] V. Desai, C. Rao, T. Kosel, and N. Fiore, 'Effect of Carbide Size on the Abrasion of Cobalt-Base Powder Metallurgy Alloys', *Wear*, vol. 94, no. 1, pp. 89–101, 1984.

[132] L. Huei-Long, L. Wun-Hwa, and S. Chan, 'Abrasive Wear of Powder Metallurgy Al Alloy 6061-SiC Particle Composites', *Wear*, vol. 159, no. 2, pp. 223–231, 1992.

[133] H. Saito, A. Iwabuchi, and T. Shimizu, 'Effects of Co Content and WC Grain Size on Wear of WC Cemented Carbide', *Wear*, vol. 261, no. 2, pp. 126–132, 2006.

[134] S. Landwehr, G. Hilmas, W. Fahrenholtz, I. Talmy, and S. DiPietro, 'Microstructure and Mechanical Characterization of ZrC–Mo Cermets Produced by Hot Isostatic Pressing', *Mater. Sci. Eng. A*, vol. 497, no. 1–2, pp. 79–86, 2008.

[135] K. Chan, Y. Lee, D. Nicolella, B. Furman, S. Wellinghoff, and R. Rawls, 'Improving Fracture Toughness of Dental Nanocomposites by Interface Engineering and Micromechanics', *Eng. Fract. Mech.*, vol. 74, no. 12, pp. 1857–1871, 2007.

[136] X. Chen, S. Wu, and J. Zhou, 'Influence of Porosity on Compressive and Tensile Strength of Cement Mortar', *Constr. Build. Mater.*, vol. 40, pp. 869–874, 2013.

[137] M. Chmielewski, J. Dutkiewicz, D. Kalinski, L. Litynska-Dobrzynska, K. Pietrzak, and A. Strojny-Nedza, 'Microstructure and Properties of Hot-Pressed Molybdenum-Alumina Composites', *Arch. Metall. Mater.*, vol. 57, no. 3, pp. 687–693, 2012.

[138] R. Rice, 'Comparison of Stress Concentration Versus Minimum Solid Area Based Mechanical Property-Porosity Relations', *J. Mater. Sci.*, vol. 28, no. 8, pp. 2187–2190, 1993.

[139] R. Spriggs, 'Expression for Effect of Porosity on Elastic Modulus of Polycrystalline Refractory Materials, Particularly Aluminum Oxide', *J. Am. Ceram. Soc.*, vol. 44, no. 12, pp. 628–629, 1961.

[140] Z. Chen, X. Wang, F. Giuliani, and A. Atkinson, 'Fracture Toughness of Porous

Material of LSCF in Bulk and Film Forms', *J. Am. Ceram. Soc.*, vol. 98, pp. 2183–2190, 2015.

[141] A. Wagh, J. Singh, and R. Poeppel, 'Dependence of Ceramic Fracture Properties on Porosity', *J. Mater. Sci.*, vol. 28, no. 13, pp. 3589–3593, 1993.

[142] R. Hardin and C. Beckermann, 'Effect of Porosity on Deformation, Damage, and Fracture of Cast Steel', *Metall. Mater. Trans. A*, vol. 44, no. 12, pp. 5316–5332, 2013.

[143] M. Aghajanian, N. MacMillan, C. Kennedy, S. Luszcz, and R. Roy, 'Properties and Microstructures of Lanxide $Al_2O_3$-Al Ceramic Composite Materials', *J. Mater. Sci.*, vol. 24, no. 2, pp. 658–670, 1989.

[144] S. Santhosh Kumar, M. Devaiah, V. Rajasekharan, T. Devaiah, T. Santhosh Kumar, and T. Seshu Bai, 'Mechanical Properties of $SiC_p$ /$Al_2O_3$ Ceramic Matrix Composites Prepared by Directed Oxidation of an Aluminum Alloy', *Ceram. Int.*, vol. 38, no. 2, pp. 1139–1147, 2012.

[145] P. Deshpande and R. Lin, 'Wear Resistance of WC Particle Reinforced Copper Matrix Composites and the Effect of Porosity', *Mater. Sci. Eng. A*, vol. 418, no. 1–2, pp. 137–145, 2006.

[146] M. Gui, S. Kang, and J. Lee, 'Influence of Porosity on Dry Sliding Wear Behavior in Spray Deposited Al-6Cu-Mn/$SiC_p$ Composite', *Mater. Sci. Eng. A*, vol. 293, no. 1–2, pp. 146–156, 2000.

[147] O. Yilmaz and S. Buytoz, 'Abrasive Wear of $Al_2O_3$-Reinforced Aluminium-Based MMCs', *Compos. Sci. Technol.*, vol. 61, no. 16, pp. 2381–2392, 2001.

[148] M. Khruschov, ‘Principles of Abrasive Wear’, *Wear*, vol. 28, no. 1, pp. 69–88, 1974.

[149] M. Kök, ‘Abrasive Wear of $Al_2O_3$ Particle Reinforced 2024 Aluminium Alloy Composites Fabricated by Vortex Method’, *Compos. Part A Appl. Sci. Manuf.*, vol. 37, no. 3, pp. 457–464, 2006.

[150] S. Tjong and K. Lau, ‘Abrasive Wear Behavior of $TiB_2$ Particle-Reinforced Copper Matrix Composites’, *Mater. Sci. Eng. A*, vol. 282, no. 1, pp. 183–186, 2000.

[151] G. Pürçek, T. Savaşkan, T. Küçükömeroğlu, and S. Murphy, ‘Dry Sliding Friction and Wear Properties of Zinc-Based Alloys’, *Wear*, vol. 252, no. 11–12, pp. 894–901, 2002.

[152] E. Rabinowicz, ‘Friction and Wear of Materials’, *Second Edition.* New York, New York Wiley, 1995.

[153] S. Hsu, M. Shen, and A. Ruff, ‘Wear Prediction for Metals’, *Wear Met.*, vol. 30, no. 5, pp. 377–383, 1997.

[154] J. Archard and W. Hirst, ‘The Wear of Metals under Unlubricated Conditions’, *Proc. R. Soc. London.Series A, Math. Phys. Sci.*, vol. 236, no. 1206, pp. 397–410, 1956.

[155] M. Karamiş and D. Odabaş, ‘A Simple Approach to Calculation of the Sliding Wear Coefficient for Medium Carbon Steels’, *Wear*, vol. 151, no. 1, pp. 23–34, 1991.

[156] N. Ma, L. Guo, Z. Cheng, H. Wu, F. Ye, and K. Zhang, ‘Improvement on Mechanical Properties and Wear Resistance of HVOF Sprayed WC-12Co Coatings by Optimizing Feedstock Structure’, *Appl. Surf. Sci.*, vol. 320, p. 364, 2014.

[157] A. Evans and T. Wilshaw, ‘Quasi-Static Solid Particle Damage in Brittle Solids—I. Observations Analysis and Implications’, *Acta Metall.*, vol. 24, no. 10, pp. 939–956,

1976.

[158] E. Rabinowicz, L. Dunn, and P. Russell, ‘A Study of Abrasive Wear under Three-Body Conditions’, *Wear*, vol. 4, no. 5, pp. 345–355, 1961.

[159] C. Jin, C. Onuoha, Z. Farhat, G. Kipouros, and K. Plucknett, ‘Reciprocating Wear Behaviour of TiC-Stainless Steel Cermets’, *Tribol. Int.*, vol. 105, pp. 250–263, 2017.

[160] C. Kuforiji and M. Nganbe, ‘Modelling the Effects of Microstructure, Properties and Abrasion Conditions on the Wear Resistance of SS316L-$Al_2O_3$ Composites’, *Tribol. Int.*, vol. 111, pp. 100–106, 2017.

[161] K. Zum Gahr, ‘Modelling of Two-Body Abrasive Wear’, *Wear*, vol. 124, no. 1, pp. 87–103, 1988.

[162] R. Richardson, ‘The Maximum Hardness of Strained Surfaces and the Abrasive Wear of Metals And Alloys’, *Wear*, vol. 10, no. 5, pp. 353–382, 1967.

[163] E. Rabinowicz and A. Mutis, ‘Effect of Abrasive Particle Size on Wear’, *Wear*, vol. 8, no. 5, pp. 381–390, 1965.

[164] M. Thakare, J. Wharton, R. Wood, and C. Menger, ‘Effect of Abrasive Particle Size and the Influence of Microstructure on the Wear Mechanisms in Wear-Resistant Materials’, *Wear*, vol. 276–277, pp. 16–28, 2012.

[165] H. Sin, N. Saka, and N. Suh, ‘Abrasive Wear Mechanisms and the Grit Size Effect’, *Wear*, vol. 55, no. 1, pp. 163–190, 1979.

[166] M. Moore and R. Douthwaite, ‘Plastic Deformation Below Worn Surfaces’, *Metall. Trans. A*, vol. 7, no. 12, pp. 1833–1839, 1976.

[167] P. Okonkwo, G. Kelly, B. Rolfe, and M. Pereira, ‘The Effect of Sliding Speed on the

Wear of Steel-Tool Steel Pairs', *Tribol. Int.*, vol. 97, pp. 218–227, 2016.

[168] I. Hussainova, J. Pirso, M. Antonov, K. Juhani, and S. Letunovitš, 'Erosion and Abrasion of Chromium Carbide Based Cermets Produced by Different Methods', *Wear*, vol. 263, no. 7, pp. 905–911, 2007.

[169] S. Kumar and V. Balasubramanian, 'Developing A Mathematical Model to Evaluate Wear Rate of AA7075/$SiC_p$ Powder Metallurgy Composites', *Wear*, vol. 264, no. 11–12, pp. 1026–1034, 2008.

[170] J. Pirso, M. Viljus, K. Juhani, and S. Letunovitš, 'Two-Body Dry Abrasive Wear of Cermets', *Wear*, vol. 266, no. 1–2, pp. 21–29, 2009.

[171] J. Pirso, M. Viljus, K. Juhani, and M. Kuningas, 'Three-Body Abrasive Wear of TiC–NiMo Cermets', *Tribol. Int.*, vol. 43, no. 1–2, pp. 340–346, 2010.

[172] J. Guilemany, S. Dosta, J. Nin, and J. Miguel, 'Study of the Properties of WC-Co Nanostructured Coatings Sprayed by High-Velocity Oxyfuel', *J. Therm. Spray Technol.*, vol. 14, no. 3, pp. 405–413, 2005.

[173] K. Jia and T. Fischer, 'Sliding Wear of Conventional and Nanostructured Cemented Carbides', *Wear*, vol. 203–204, pp. 310–318, 1997.